



Structure and kinematics of active faulting in the Hope-Kelly and Alpine Fault intersection zone, South Island, New Zealand

Jessie L. Vermeer^{a,*}, Mark C. Quigley^a, Brendan G. Duffy^a, Robert M. Langridge^b, Jarg R. Pettinga^c

^a University of Melbourne, Parkville, Victoria 3010, Australia

^b GNS Science, Lower Hutt, New Zealand

^c University of Canterbury, Christchurch, New Zealand

ARTICLE INFO

Keywords:

Hope fault
Kelly fault
Alpine fault
Fault intersection
Strike-slip

ABSTRACT

Using lidar, photogrammetry and field studies, we investigate the structure and kinematics of the Hope, Kelly, and Alpine faults where they converge and intersect along the Australian-Pacific plate boundary in New Zealand. Approximately 50% of the reverse-dextral slip rate of the Alpine fault in the west transfers to the dextral central Hope Fault in the east via a horsetail splay zone of distributed oblique dextral-normal shear forming the Hope-Kelly fault system. The westernmost portion of the Hope fault is misoriented for dextral slip and is likely an extensional fault that accommodates the Alpine fault slip rate change across the intersection zone. As it transitions to an extensional fault, most of the strike-slip of the Hope fault is transferred southward onto Kelly fault strands via incipient, linking fault domains of coeval NE-SW and EW-striking dextral faults. The transition from the narrow zone defining the central Hope Fault to dispersed horsetail splays of the Hope-Kelly fault system is located immediately above the eastward down-dip projection of the Alpine Fault at the base of the seismogenic zone. This suggests that structural interactions among these faults within seismogenic depths control surface rupture geometries and kinematics. Coeval intermingling of surface rupture traces transecting latest Pleistocene to Holocene landforms indicates ongoing structural interactions in active faulting at the intersection of the Hope-Kelly fault splays with the Alpine fault. The transition from dextral to dextral normal kinematics on the horsetail splay accommodates differential orogenic growth through geometrically and kinematically efficient faulting that allows extension of the Alpine fault hanging wall parallel to strike, enabling the slip rate change between the central and northern Alpine fault sections.

1. Introduction

Analysis of the structure and kinematics of intersection zones between active plate boundary faults can improve understanding of earthquake rupture dynamics (Robinson, 2004; Parsons et al., 2012; Schwartz et al., 2012; Hamling et al., 2017; Holden et al., 2017; Nicol et al., 2018) and the roles of fault interactions in orogenic development (Wakabayashi et al., 2004; Lock et al., 2006; Landgraf et al., 2009; Niemi et al., 2013). The nature of fault intersections influences fault geometries and structural styles of deformation, kinematics, slip rates, strain accumulation, and earthquake processes, such as rupture propagation and stress transfer, that in turn affect earthquake frequency-magnitude distributions (Spotila and Anderson, 2004; Mouslopoulou et al., 2007a, b; Rosas et al., 2012; Schwartz et al., 2012; Quigley et al., 2019). Faults

may be kinematically linked such that slip on one fault is transferred onto the other; by direct geometric linkage or ductile deformation (e.g., slip transfer between sub-parallel strike-slip faults) (Schwartz et al., 2012; McGill et al., 2013). Geometric linkage comprises main fault planes that abut or intersect; the angle of intersection between the faults and the kinematics of each fault affects whether strain in the upper crust can be accommodated by rigid block motions. If the intersection between the faults is parallel to the slip vector of both faults, then the faults can be considered to have a neutral intersection as defined in Peacock et al. (2017). If the slip vectors are not parallel and/or the slip vector of the fault changes across the intersection, the faults may be connected via relative neutral intersection, where the vector of slip deficit on one fault is accommodated by differential slip on the intersecting fault. Alternatively, a diffuse intersection zone may form where the principal faults

* Corresponding author.

E-mail address: jvermeer@student.unimelb.edu.au (J.L. Vermeer).

<https://doi.org/10.1016/j.tecto.2021.228928>

Received 4 September 2020; Received in revised form 30 April 2021; Accepted 9 May 2021

Available online 15 May 2021

0040-1951/© 2021 Elsevier B.V. All rights reserved.

are replaced by smaller structures such as a fractal system of fault planes and rigid motion of small blocks, and/or deformation accommodated by volume changes (vein formation, dissolution, folding). Finally, the temporal development of a fault intersection is critical in understanding its kinematic and geometric significance. Relevant questions include: do the faults have different histories, at what stage in fault evolution did the faults begin to interact and intersect, how much total slip or strain has been accommodated, and what implications do these aspects have for structural evolution of fault zones and hazard characterization?

Fault intersections have been studied at many spatial and temporal scales using a variety of field, computational, and analogue modeling techniques (e.g. Sieh et al., 1993; Ando et al., 2004; Mouslopoulou et al., 2007a, 2007b; Dooley and Schreurs, 2012; Žalohar, 2012; Duffy et al., 2013; Peacock et al., 2017; Fedorik et al., 2019; Quigley et al., 2019; van Gent and Urai, 2020). In the North Island of New Zealand, where the dextral strike-slip North Island Fault System intersects with the Taupo Rift, strain is accommodated by gradual changes in fault orientation and kinematics creating a stable, efficient transition between strike-slip and normal fault systems (Mouslopoulou et al., 2007a, 2007b). In southern California, some dextral strike-slip faults with strikes differing by up to 30° do not geometrically intersect, but the faults bend and change orientation along strike to become subparallel and enable slip transfer through inter-fault domains via distributed deformation on cross faults or folds (e.g. Morton and Matti, 1993; Zachariassen and Sieh, 1995). In some cases, sub-parallel strike-slip faults that do not meet at the surface may converge at depth into a single fault zone (e.g. Graymer et al., 2007; Chaussard et al., 2015). In Alaska, the dextral strike-slip Denali and

Totschunda faults are near vertical and are geometrically and kinematically linked with a direct connection of the two faults, that allows earthquake rupture to propagate directly across the intersection (Haeussler et al., 2004; Schwartz et al., 2012). In the Gulf of Cadiz, at the intersection between active strike-slip and thrust faults, slip transfer is accomplished via a complex process zone where strike-slip faults and thrust faults merge both geometrically and kinematically, accommodating a common horizontal slip vector on dextral, oblique, and thrust faults with strikes ranging by up to 120° (Rosas et al., 2012; Rosas et al., 2015).

Previous regional scale (1:250,000) mapping indicates that the junction between the Alpine fault in the west and the central Hope fault to the east is defined by the Taramakau section of the Hope fault, the Kelly fault, and associated subsidiary faults in a horsetail-like structure (Fig. 1 and 2A) (Freund, 1971; Nathan et al., 2002; Berryman et al., 2003; Langridge and Berryman, 2005). Detailed mapping and structural analysis have proven challenging in this steep, heavily vegetated, and remote mountainous terrain, however, recent lidar surveys have enabled higher resolution mapping and kinematic analysis of surface ruptures in nearby areas of the western Southern Alps (Barth et al., 2012; Langridge et al., 2014; Khajavi et al., 2014; Khajavi et al., 2016). Kinematic studies and Holocene slip rate balancing confirm that ~50% of the central Alpine fault slip is transferred onto the central Hope fault and ~50% continues past the Hope Fault junction on the northern Alpine fault (Langridge et al., 2010). Although the Hope and Alpine faults have been studied by numerous researchers, the geometry, kinematics, and mechanical significance of the intersection zone between

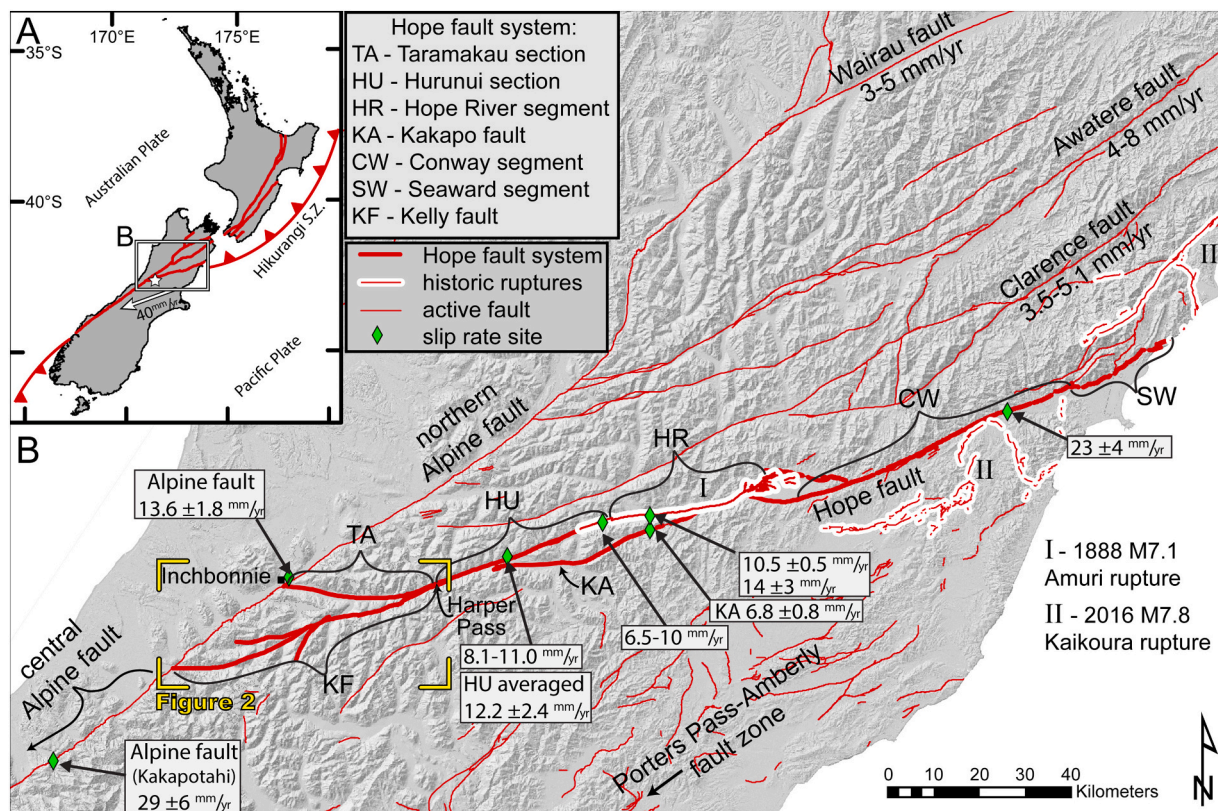


Fig. 1. A) Tectonic setting of New Zealand showing the major faults delineating the boundary between the Australian and Pacific plates. The white star indicates the study area and location of the displayed Pacific plate motion (white arrow, 40 mm/yr at 251°) relative to the Australian plate (Altamimi et al., 2016). B) Map of the southern Marlborough fault system (MFS) with hillshade topography. Generalized slip rates of the Wairau fault, Awatere fault and Clarence fault are shown (Mason et al., 2006; Zachariassen et al., 2006; van Dissen and Nicol, 2009). Geometric segments and slip rate sites (green diamonds) are shown for the Hope Fault (bold) and relevant sites on the Alpine fault (Cowan, 1990; Yang, 1991; Cowan and McGlone, 1991; Norris and Cooper, 2001; Langridge et al., 2003; Langridge and Berryman, 2005; Langridge et al., 2010; Khajavi et al., 2016; Khajavi et al., 2018). The Kelly fault branches off the Hope fault at Harper Pass. Historic earthquake ruptures involving the Hope fault are highlighted: the 1888 M ~ 7.1 Amuri earthquake (I), and the 2016 Mw7.8 Kaikoura earthquake (II) (Langridge et al., 2016). (For interpretation of the references to colour in this figure legend, the reader is referred to the web version of this article.)

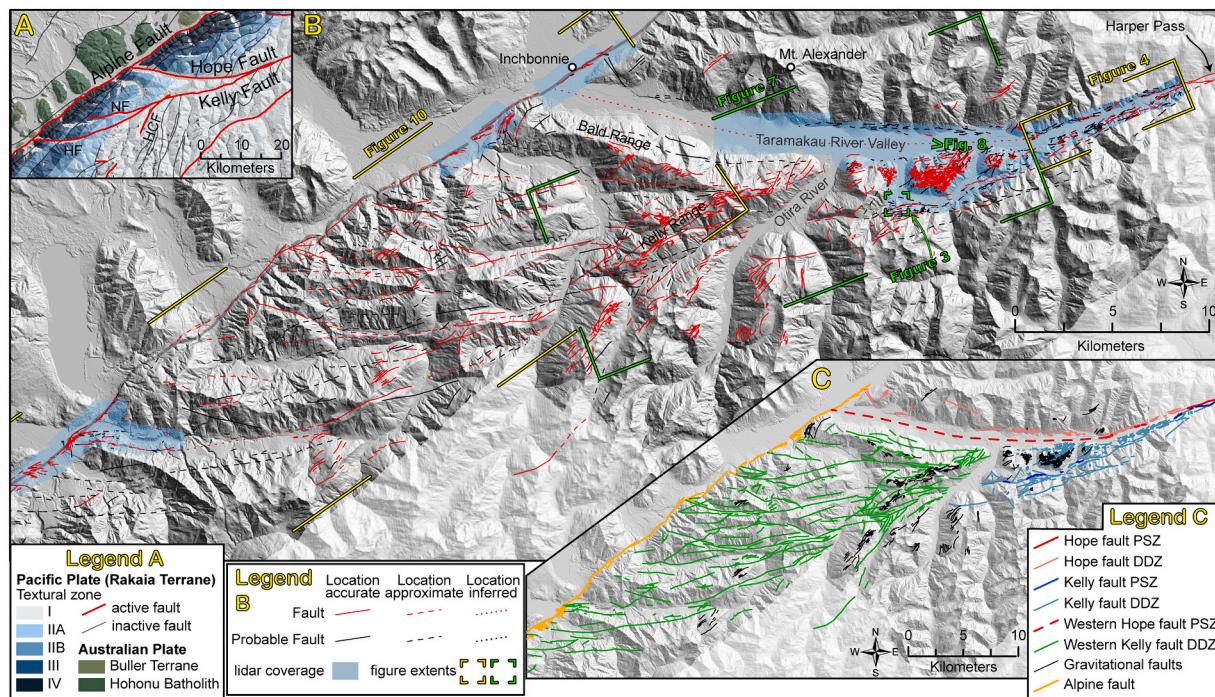


Fig. 2. A) Prior mapping of the Taramakau section of the Hope fault and the Kelly fault (Freund, 1971; Berryman et al., 1992; Nathan et al., 2002; Langridge et al., 2016). The Hope fault was mapped passing down the Taramakau Valley, and the Kelly fault is the linear continuation of the central Hope fault, striking roughly parallel to the plate motion (Langridge and Berryman, 2005). The Kelly fault is further subdivided into the Hunts Creek fault (HCF), Newton fault (NF), and Hura fault (HF) (Berryman et al., 1992; Langridge et al., 2016). Relevant bedrock mapping and mapped inactive faults are also shown, including the metamorphic textural zones of the Pacific plate east of the Alpine fault, and the Australian plate granitoids west of the Alpine fault (Nathan et al., 2002). B) New mapping presented in this study from Harper Pass to the Alpine fault, symbolized by fault certainty and location accuracy (see legend and methods for more details). Blue shading indicates lidar coverage. Dark gray hillshade indicates Photogrammetric DSM (pDSM) coverage (West Coast Regional Council, 2017). Background light gray hillshade is 30 m ALOS DSM (<https://www.eorc.jaxa.jp/ALOS/en/aw3d30/index.htm>). The extent of Figs. 3, 4, 7 and 10 are shown with yellow or green corner marks. C) New mapping with faults colored according to the name. All faults and probable faults are displayed with solid lines. (For interpretation of the references to colour in this figure legend, the reader is referred to the web version of this article.)

these faults has remained poorly understood (Fig. 2A).

In this study, we use new lidar- and photogrammetry-derived digital elevation models to map the surface expression of the Taramakau section of the Hope fault and the Kelly fault, from Harper Pass in the east to their intersection with the Alpine fault in the west (Fig. 2B). We present the locations, orientations, and kinematics of faults in this dense and complex network as revealed by the new mapping. The general structure is manifested as a horsetail splay (Fig. 2A), as identified by previous authors (Freund, 1971; Nathan et al., 2002; Berryman et al., 2003; Langridge and Berryman, 2005), but with significantly more structural and kinematic complexity than previously identified. Fault strike and kinematics systematically transition from plate motion parallel (strike $\sim 070^\circ$) with dextral slip at Harper Pass, to sub-perpendicular to the Alpine fault (strike $090 \pm 10^\circ$) with normal-dextral kinematics in the west at the intersection with the Alpine fault (Fig. 2B). To understand how this fault system transfers slip between the Alpine and Hope faults, we use our detailed mapping to inform 3D structural models for visualization of the structure, and we use analog modeling to better characterize the kinematics. These models reveal that simple parent fault geometry gives rise to this complex intersection process zone that is kinematically and geometrically distinct from the parent faults, but efficiently transfers slip between them.

2. Geologic setting

New Zealand straddles the boundary between the Australian plate in the west and Pacific plate in the east (Fig. 1). The plate boundary on the South Island is primarily defined by the Alpine fault and Marlborough Fault System (MFS), which connect the Puysegur subduction zone in the

south to the Hikurangi subduction zone in the north. Subsidiary on-land fault systems in the central to northern South Island include the Main Divide Fault Zone (MDFZ), Canterbury fold and thrust belt, and the Porters Pass-Amberly fault zone, all located within the Pacific Plate, east of the Alpine fault and south of the MFZ.

The Alpine fault is a northeast-striking, southeast-dipping, dextral-reverse fault that separates Australian Plate rocks in the footwall from the Pacific Plate rocks in the hanging wall. The reverse component of slip on the Alpine fault has resulted in exhumation of the Pacific Plate rocks, exposing lower crustal metamorphic zones that are high grade mylonite and schist closest to the Alpine fault and decrease in grade to the east (Fig. 2A) (Nathan et al., 2002; Cox and Barrell, 2007). The protolith rocks are Rakaia Terrane, with Aspiring Lithologic Association schist closest to the Alpine fault and Torlesse Greywacke with bands of mudstone and chert further east (Nathan et al., 2002; Rattenbury et al., 2006; Cox and Barrell, 2007). The metamorphic textural zones strike subparallel to the Alpine fault and have generally southeast-dipping fabrics, but both the structures and thicknesses vary along strike (Nathan et al., 2002; Cox and Barrell, 2007). The Alpine fault surface trace is remarkably straight at the continental scale but at the km-scale exhibits a zig-zag surface trace that alternates thrust and dextral dominant segments 1–10 km in length relating to structural interactions in the uppermost 1–2 km of crust (e.g. Norris and Cooper, 1995; Barth et al., 2012). The Alpine fault is divided into 5 segments along the length based on changes in structure, kinematics and slip rate (Berryman et al., 1992; Norris and Cooper, 2001; Barth et al., 2013).

The Alpine fault sections relevant to this study are the central section and the northern sections, the boundary between which is at the Toaroha River, near where the Kelly fault meets the Alpine fault (Fig. 1B)

(Berryman et al., 1992; Barth et al., 2013). The central section is south of the Kelly fault intersection and is the dominant tectonic structure in the central South Island with a maximum strike-slip rate of 29 ± 6 mm/yr and maximum dip-slip of >12 mm/yr, which is $\sim 80\%$ of the total relative plate motion (Norris and Cooper, 2001; Sutherland et al., 2007; Wallace et al., 2007; Barth et al., 2013; Howarth et al., 2018). The remaining relative plate motion is accommodated on lower slip rate fault systems (Pettinga et al., 2001), including the Main Divide fault zone, a west-dipping oblique thrust fault system that is antithetic to the Alpine fault, located parallel to the Alpine fault and east of it within the Southern Alps (Cox and Findlay, 1995; Becker and Craw, 2000; Cox et al., 2012). North of the Alpine-Kelly fault intersection is the northern section of the Alpine fault, which has similar orientation and kinematics as the central section, but a lower slip rate that decreases to the north as slip is transferred onto the various splays of the MFS. The slip rate is the fastest at the southern end with 14 ± 2 mm/yr dextral strike-slip and 3.4 ± 0.6 mm/yr reverse at Inchbonnie that decreases to 10 ± 2 mm/yr dextral and 1.3 ± 0.5 mm/yr reverse at the intersection of the Alpine and Awatere faults (Langridge et al., 2010; Langridge et al., 2017). At the north end, the Wairau fault, considered to be the northward continuation of the Alpine fault but also a member of the MFS, has only 3 ± 0.5 mm/yr dextral slip rate as most of the relative plate motion has been transferred onto the other MFS faults (Knuepfer, 1992; Langridge et al., 2010; Langridge et al., 2017; Zachariassen et al., 2006).

The MFS is a series of dextral faults that strike northwest and transfer slip between the Alpine fault and the Hikurangi Subduction Zone (Van Dissen and Yeats, 1991; Barnes and Audru, 1999; Norris and Cooper, 2001; Langridge et al., 2010; Langridge et al., 2003; Yang, 1991; Khajavi et al., 2016; Cowan and McGlone, 1991; Cowan, 1990; Khajavi et al., 2018; Langridge and Berryman, 2005). These faults are all east of the Alpine fault and contained within the Pacific Plate Rakaia Terrane rocks (Nathan et al., 2002; Rattenbury et al., 2006). There are many active and inactive faults within the MFS, but the 4 principal MFS faults, from north to south, are the Wairau, Awatere, Clarence, and Hope faults (Fig. 1). From north to south the Holocene slip rates of these faults increase (Fig. 1B), while the age of the faults is thought to decrease such that the Wairau is the oldest and slowest slipping, while the Hope is the youngest and fastest slipping.

The Hope fault is interpreted to have initiated 0.6–1.6 Mya, based on applying Holocene slip rates to displaced bedrock units (Wood et al., 1994; Langridge et al., 2013). It extends from the Alpine fault near the boundary between the central and northern sections in the west to the Hikurangi Subduction Zone in the east (Litchfield et al., 2014; Stirling et al., 2012). Geometric complexities on the Hope fault, including step-overs and bends, are used to divide the fault into 5 geometric segments and two branching faults (the Kelly Fault and the Kakapo Fault) (Fig. 1B) (Freund, 1971; Cowan, 1989; Cowan and McGlone, 1991; Langridge and Berryman, 2005). Segments strike $064\text{--}084^\circ$ but the overall strike of the fault system is $\sim 080^\circ$, and it is overall a dextral strike-slip fault. At the intersection of the Hope and Alpine faults, the vector of the Pacific plate relative to the Australian plate is 40 mm/yr at 260° (Altamimi et al., 2016) and the principal horizontal stress (PHS) inferred from bedrock structures and historic seismicity is oriented 116.2° ($-14.9/+14.3$) (Nicol and Wise, 1992; Pettinga and Wise, 1994; Michailos et al., 2020). The Hope fault is the fastest slipping of the major MFS faults (Fig. 1), and slip rate varies along its length. The slip rate on the easternmost Seaward segment is unknown. The Conway segment near the eastern end of the fault has the fastest known slip rate, up to 23 ± 4 mm/yr of dextral slip focused on a single, relatively narrow principal slip zone (Eusden et al., 2000, 2005; Langridge et al., 2003; Manighetti et al., 2015). The Hurunui and Hope River segments have a lower slip rate, but when combined with the slip on the branching subparallel Kakapo fault, they accommodate a similar total slip rate to the Conway segment (Cowan, 1990; Cowan and McGlone, 1991; Yang, 1991; Langridge and Berryman, 2005; Khajavi et al., 2016; Khajavi et al., 2018). In this paper, we refer to the Hurunui and Hope River segments, along with the Kakapo fault, as

the “central Hope fault”.

The westernmost section of the Hope fault is the Taramakau section, which follows the Taramakau River valley from Harper Pass to the Alpine fault near Inchbonnie (Freund, 1971; Nathan et al., 2002; Langridge and Berryman, 2005). The western 10–15 km of the Taramakau section is inferred to follow the Taramakau River valley, primarily based on the linearity and morphologic prominence of the wide valley and the apparent 4–5 km dextral displacements of the Alpine fault subparallel metamorphic textural zones across the valley (Freund, 1971; Nathan et al., 2002) (Fig. 2A). This section of the fault system strikes $\sim 090^\circ$, a deviation $\sim 20^\circ$ clockwise from the overall Hope fault strike; it is misoriented for dextral strike-slip. The Kelly fault branches off the south side of the Hope fault at Harper Pass and continues along the straight line projection of the central Hope fault ($\sim 070^\circ$) southwest to meet the Alpine fault near the Toaroha and Styx Rivers (Nathan et al., 2002; Berryman et al., 2003; Langridge and Berryman, 2005). Small <1 km apparent dextral displacements of the metamorphic zones have also been mapped along the Kelly fault trace, which crosses multiple rivers and ridges and has no large scale morphologic features (i.e. no fault parallel river valley) (Nathan et al., 2002; Berryman et al., 2003; Langridge and Berryman, 2005). The Kelly fault is further subdivided into the Hunt Creeks fault, Newton fault and Hura fault (Fig. 2a) (Berryman et al., 2003; Langridge et al., 2016). In this paper, we will refer to the “Hope-Kelly fault system” as including all active or apparently active faults between Harper Pass and the Alpine fault (i.e. the Taramakau section of the Hope fault, the Kelly, Newton, Hura and Hunt creek faults, and all the newly mapped splays of these faults). The slip rate of Taramakau section and Kelly fault are unknown. When resolved into horizontal net slip vectors, the slip rate of the central Alpine fault is matched by the slip rate on the central Hope fault combined with the northern Alpine fault (Langridge et al., 2010). The prevailing hypothesis is that the central Alpine fault slip is partitioned between the northern Alpine fault and the Hope fault, and that the slip is transferred to the central Hope fault through the Kelly fault and the Taramakau section of the Hope fault, though the exact nature of this slip transfer is unknown.

The study area lies entirely west of the Main Divide of the Southern Alps, a geomorphically active region with steep terrain and thick vegetation. The Southern Alps are considered to be in long term steady state, with denudation rates balancing tectonic uplift (Adams, 1980; Hovius et al., 1997). Rock uplift is driven by reverse motion on the Alpine fault; uplift rates determined from GPS are up to 8 mm/yr, and geologically determined uplift rates are up to 11 mm/yr (Adams, 1980; Beavan et al., 2004; Little et al., 2005). A strong orographic effect causes the western side of the Southern Alps to get up to ~ 12 m of annual precipitation with up to 7 m/yr in the study area (Tait et al., 2006) that drives fluvial and chemical erosional processes and supports the dense temperate rainforest vegetation. Landsliding, rockfalls, and other mass wasting processes, contribute to a long-term average of 4–9 mm/yr of denudation, and the rate temporarily increases following proximal earthquakes (Hovius et al., 1997; Yang, 1992; Korup et al., 2007; Korup et al., 2004; Allen et al., 2011; Robinson et al., 2016; Rosser and Carey, 2017). Being at the intersection between the Hope and Alpine faults, the study area is situated in the highest earthquake hazard zone in New Zealand, with 475-yr (0 to 1 s) spectral accelerations of >0.7 to >1.2 g (Stirling et al., 2012) and is regularly subject to moderate to large magnitude earthquakes. The Alpine fault produces large magnitude earthquakes every ~ 300 years, up to $\sim M8$ (e.g. Howarth et al., 2018). The central Hope fault paleoseismic record indicates $\sim M7$ surface rupturing earthquakes every $\sim 266 \pm 100$ yr, the most recent was the 1888 $M7\text{--}7.3$ Amuri earthquake (McKay, 1890; Cowan, 1990; Khajavi et al., 2018). Historic earthquakes nearby include the 1929 $M7.1$ Arthurs Pass earthquake, 1994 $M6.8$ Arthurs Pass earthquake, and the 2015 $M6.0$ Wilberforce earthquake (Arnadottir et al., 1995; Berryman and Villamor, 2004; Rosser and Carey, 2017). Quaternary glaciations have formed U-shaped glacial valleys that are now occupied by braided rivers, postglacial alluvium and alluvial fans (Nathan et al., 2002;

Barrell et al., 2011). The Last Glacial Maximum was ~21 ka and rapid deglaciation saw complete glacial retreat from the study area by ~15 ka (Ivy-Ochs et al., 1999; Barrows et al., 2013; Eaves et al., 2017; Shulmeister et al., 2019). The uplift of the Southern Alps is matched by high mass-wasting denudation rate and annual precipitation creating a dynamic landscape that has potential to quickly erode and refresh landforms used to map active faults and surface rupture, such as fault scarps and displaced fluvial features (Cox et al., 2012).

3. Fault and geomorphic mapping methods

3.1. Data

In this study, we use light detection and ranging (lidar) data, a photogrammetric digital surface model (pDSM), 30 m ALOS digital surface model (30 m DSM), orthorectified airphoto datasets, and field studies to undertake detailed mapping. The lidar (Fig. 2B) was flown in September 2015 by AAM Pty. Ltd. (<http://www.aamgroup.com/>) using a Rigel Q1560 at 390–400 kHz pulse rate. Vertical accuracy is ± 0.15 m and horizontal accuracy is ± 0.50 m with laser footprint size 0.24–0.39

m. The data were delivered as LAS datasets classified as ground and non-ground returns; classification was completed by AAM using algorithms appropriate for the vegetation type then manually checked.

The lidar along the Alpine fault was gridded into a 1 m bare earth DEM using inverse distance weighted (IDW) interpolation on the ground returns with a variable search radius of 20 m and 12 points. For the lidar along the Taramakau and Styx Rivers we determined appropriate DEM grid resolution using the formula from Langridge et al. (2014): “ $s = \sqrt{A/n}$ ” where s is the cell size, n is the number of sample points and A is the area containing the sample points.” We determined that the lidar has sufficient ground returns to be gridded at 1.5 m, and all but the most heavily vegetated areas have sufficient ground returns for 0.5 m resolution. Occasional gaps in the data are larger than 1.5 m but some of these have been correlated to large tree trunks during field investigations. Using nearest neighbor interpolation, we made DEMs at both 0.5 and 1.5 m resolution. We generally used the 0.5 m DEM and derivatives for analysis but check for artifacts by regularly comparing the mapping to the 1.5 m DEM and derivatives.

The photogrammetric digital surface model (pDSM) supplied by the West Coast Regional Council was produced by Aerial Surveys in 2017

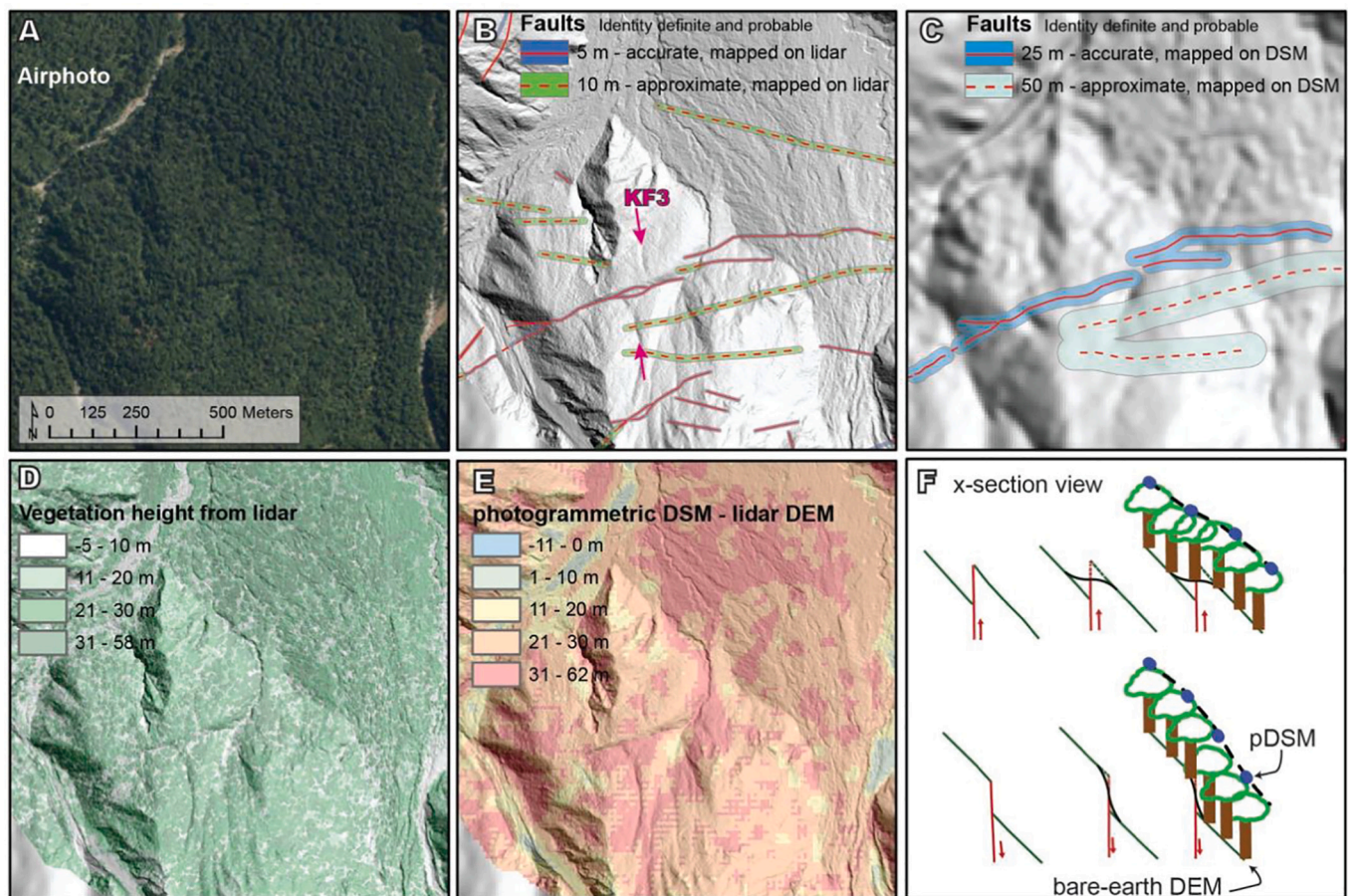


Fig. 3. Compilation of data types used in this study, location shown on Fig. 2. Site is west of Lake Kaurapataka. A) Airphoto of the same extent as B–E. Shows how heavily vegetated the landscape is and how fault scarps are not obvious. B) Hillshade of lidar derived 1.5 m bare earth DEM and faults mapped on it. The spatial accuracy of accurate and approximate fault traces is shown by the extent of the colored buffers. Displacement measurement KF3 is shown in pink. C) Hillshade of pDSM and spatial accuracy of fault traces that can be mapped with this data. Despite the limitations, pDSM does accurately represent large-scale topographic features and the faults with sufficient displacement can be identified. Buffers show the spatial accuracy of fault traces mapped using the pDSM, which have much larger inaccuracy than faults mapped on the lidar DEM. D) Vegetation height extracted from the lidar data. Shows areas of highest trees and bare stream channels. Most forest at this site is greater than 30 m tall. E) Elevation difference between pDSM and lidar bare earth DEM. The largest difference between the two datasets is in areas of tall trees (see D), and across narrow topographic depressions where a combination of vegetation cover and possibly aliasing makes the pDSM surface higher than the DEM surface. F) schematic cross sectional slope profiles illustrating how tree cover and larger grid size result in topographic model in which small, sharp features are subdued or completely unidentifiable and only features with large total elevation change are identifiable. (For interpretation of the references to colour in this figure legend, the reader is referred to the web version of this article.)

from aerial photography collected at 0.3 m resolution using Vexcel's digital UCE camera at 5769 m flight height (West Coast Regional Council, 2017). The pDSM was created by Aerial Surveys using automated pixel matching and auto-correlation; the final pDSM has a 9 m grid resolution. The pDSM represents the top of dense vegetation, not the bare earth; to understand how this affects our interpretation of geomorphic features we compare the pDSM to lidar-derived bare earth DEMs where they overlap (Fig. 3). We find the difference between the two surfaces is greatest in forested areas where maximum heights of mature native forest cause the pDSM to be 30–60 m higher than the bare earth lidar derived DEM (Fig. 3E). This vegetation shielding may completely obscure small landforms, limiting the size of geomorphic features that can be recognized using the pDSM and making features appear more subdued than a bare earth representation (Fig. 3F). However, large geomorphic features including fault scarps can still be mapped with the pDSM with less spatial precision or certainty of feature identity, relative to the lidar data.

We also extensively use the 0.3 m resolution orthophoto, produced from the same photos as the pDSM (Fig. 3A). Above the bush line we use orthophotos to map faults with greater accuracy than with the pDSM alone. We use the orthophotos to help delineate landslide scars, riverbeds, and anthropogenic features such as farm tracks, tramping trails, and fence lines.

For regional context outside the extent of the other datasets, we use an ALOS 30 m DEM, downloaded from <https://www.eorc.jaxa.jp/ALOS/en/aw3d30/index.htm>.

3.2. Mapping methods

Geomorphic surfaces and lineaments are mapped using the lidar derived DEMs and pDSM and derivatives of them (hillshade, slope, aspect, curvature, contours, topographic profiles). Geomorphic unit contacts are classified as accurate or approximate, which refers to the spatial precision of the line defining the mapped contact. Geomorphic units inset into other geomorphic or geologic units are mapped as distinct (e.g. a stream channel incised into an alluvial fan is mapped separately). Geologic and geomorphic map units and descriptions are listed in Table 1. In addition to geomorphic surfaces, we map landform lineaments and classify them according to interpreted origin. Mapped lines are classified according to the accuracy that we can identify their location, which is dependent on the characteristics of the feature and the elevation data coverage, as explained in Table 2 and shown in Fig. 3B and C. The geomorphic setting and characteristics of each lineament are considered when developing interpretations of the formation process (fault, terrace riser, glacial striation, cut bank, landslide head scarp, erosional bedrock feature, etc.). Lineaments that offset/deform other geomorphic features, cracks in the ground surface, linear boundaries of peat bogs/ponds, or distinct, linear breaks in slope are classified as fault or probable fault traces. The differentiation between fault and probable fault is based on the certainty of faulting origin of the lineament. If the lineament cuts and displaces a surface that can be correlated across the lineament or if there are identifiable discrete ground fractures observed on the lidar DEM, the lineament is classified as a “fault.” Lineaments are classified as “probable fault” if they lack specific definitive evidence for faulting (e.g., discrete displacements), but cannot be attributed to other geomorphic features (i.e. not a terrace riser or glacial striation). Examples of probable faults include lineaments where other features cannot be correlated across the lineament (i.e. an unusually straight terrace edge or hillslope base), lineaments that could possibly be purely erosional in origin (i.e. steepened section of hillslope that is not continuous across multiple ridges), or if the lineament is defined by an alignment of other features (i.e. linear alignment of laterally bent ridges or streams). With this classification system, each mapped fault has two independent classifications: spatial accuracy and identity certainty. Fault identity certainty and spatial accuracy are not used as a proxy for “primary or principal fault” and “secondary fault.”

Table 1
Geomorphic units, unit descriptions, and symbols.

Unit symbol	Unit name	Unit description
af	Alluvial fan	Characterized by a conical or partial conical landform of depositional origin where a stream channel exits a narrow valley.
oaf	Relict alluvial fan	Same as unit alluvial fan, but relict, with the current stream channel incised through the relict fan deposit and no longer flowing or depositing over the top of the landform. In some cases, a lower, more distal fan signals that the higher fan is inactive. Differentiated from relict terraces based on surface sloping away from the source channel roughly perpendicular to the downstream direction.
at	Alluvial terrace	Evenly sloped, nearly planar surface created by a flowing stream or river. The surface may be created by erosion or deposition. Active alluvial terraces include those that may be affected by stream channel flooding, usually the lowest terrace in a suite.
oat	Relict alluvial terrace	Same as alluvial terrace but the relict surface is above the current flood plain and is no longer affected by typical flooding. Usually terraces above the one at lowest elevation are considered relict, with only the lowest terrace being considered active. Differentiated from relict fan surfaces based on maximum slope direction being roughly parallel to the downstream flow direction of the source channel.
ac	Active stream channel	Region of active erosion and/or deposition along a stream channel, within the flood plain.
ls	Landslide	A landslide or debris flow deposit that has not been fluvially reworked. Usually characterized by a hummocky, disorganized surface and/or lobate form.
bog	Bog, pond, or closed depression	A closed or mostly closed depression that traps water, sediment and may be conducive to the formation of peat. Usually exhibits a flat surface morphology indicative of still water deposition and peat accumulation. May be vegetated or occupied by standing water, either continuously or ephemerally.
bp	Braid plain of large river	The active and recently inactive area of erosion and deposition surrounding the active river channel. These areas may at any time become re-incorporated into the active river channel because they are not raised high above the river.
clf	Cliff likely not entirely bedrock	Use to delineate erosional areas around quaternary deposits where the exposed material might not be bedrock. Used so that geomorphic units can be confined to the preserved surfaces that are useful for reconstructing geomorphic stratigraphy, rather than encompassing the whole deposit which may have a different origin than the process that formed the top surface.
bdrk	Bedrock	Areas where bedrock is exposed or likely present beneath only pedogenic soil.
relict_l	Relict landscape	Decoupled upland; area that is fluvially disconnected from the current landscape, but not specifically identified as a relict terrace or fan. May contain features such as stream channels that no longer have headwaters or are disconnected from the downstream channel by a large cliff. May contain glacial features such as striations.
oc	Old channel	An inactive channel segment, usually within a relict landscape (relict_l). Often has subdued topography with a rounded bottom, and no connection with the current fluvial system.

We classified faults (Fig. 2C) as belonging to the Hope fault principal slip zone (PSZ) or Kelly fault PSZ from Harper Pass to the Otira River where we could identify fault traces with accumulated discrete displacement greater than that expected from a single earthquake, indicating that multiple earthquakes have occurred on the same

Table 2

Fault spatial accuracy classifications on lidar and photogrammetric datasets, and morphologic characteristics of the fault surface expressions typical of each classification.

Line type	Zone width on the lidar data	Zone width on the photogrammetric DEM	Geologic significance of the line type
Accurate (solid)	5 m	25 m	Discrete fault trace.
Approximate (dashed)	10 m	50 m	Fault trace defined by a deformation zone with or without discrete surface fractures.
Inferred (dotted)	40 m	150 m	Fault not expressed at the surface due to burial or erosion, but presence is inferred, usually based on high confidence faults on either side.

structure. Surrounding fault traces without identifiable accumulated displacement are classified as Hope fault distributed deformation zone (DDZ) north of the Taramakau River and Kelly fault DDZ south of the river. A PSZ may pass along strike into a DDZ as fault structure changes. We have differentiated the Western Hope fault PSZ as the fault section inferred beneath the Taramakau River where the valley trends $\sim 090^\circ$. West of the Otira River and south of the Taramakau River, faults are classified as the Western Kelly fault DDZ. In this area it is often unclear with the current data how much finite slip has accumulated on each of these structures and if any are through going structures. We refer to the entire fault system from Harper Pass to the Alpine fault as the Hope-Kelly fault system.

Fault strike is approximated by the average trend of the mapped fault trace unless specifically noted that the strike was calculated (3-point problem) or measured in the field.

We have not expanded on the prior bedrock lithologic and structural mapping (Nathan et al., 2002). In lineament classification, we consider the potential for bedrock bedding or metamorphic foliation to produce lineaments in the landscape, an example can be seen in the north hillside of the Taramakau River valley opposite the Otira River where foliation produces a distinct lineation fabric visible in the bare earth DEM.

We conducted field investigations in 2017, 2018 and 2019 to ground truth the remote mapping, with a focus on fault traces. Where mapped 'fault traces' were revealed to be features unrelated to faulting origin (e. g., a half buried log appearing like a small fault scarp in the lidar), they were removed or reclassified. In other cases, fault rocks and shear zones were observed and included on our maps where there is no geomorphic expression, such as shear zones in active strath terraces or landslide scars. We also used tape and compass to make field measurements of fault offsets and scarp heights and made observations of fault motion indicators such as slickenlines on exposed fault surfaces. We visited $\sim 70\%$ of the mapped fault traces within the areas of lidar coverage in the Taramakau Valley and along the Alpine fault, on the Kelly Range, and within the mid-Taipo River valley.

GIS files of the complete fault and geomorphic mapping completed in this study are included in the supplemental information files.

3.3. Displacement measurements

From the mapping and field studies, we measure discrete displacements of linear geomorphic features and derive horizontal (fault strike parallel) to vertical displacement ratios (H:V). Geomorphic markers in some settings may be subject to unknown effects of geomorphic modification that precludes precise displacement measurement, such as post-fault-displacement erosion of terrace risers, or an unknown amount of deposition behind an uphill facing scarp. In these circumstances,

discrete offsets of correlative geomorphic features could not be measured with confidence, but we estimate fault kinematics with apparent displacements, which are described as such and a precise H:V ratio is not provided. The H:V ratios and apparent displacements provide only an overall sense of the obliquity of fault slip. Where possible, we used fault traces across topography to measure fault strike and dip (a 3-point problem). However, unless otherwise indicated, the H:V ratios presented here are not associated with a measurement of fault dip, so they are not true strike-slip to dip-slip ratios. Slip and slip rates at key sites are the foci of future work.

4. Mapping results

4.1. Upper Taramakau River valley

At Harper Pass, the Kelly fault branches off the Hope fault and they trend subparallel in the upper Taramakau River valley, with the Hope fault PSZ on the north side of the valley and the Kelly fault PSZ on the south side (Figs. 2 and 4). The Hope fault has discontinuous PSZ geomorphic traces consisting of dextral displacement fault scarps up to 1.5 km long where the fault cuts and displaces tributary alluvial fans extending out onto the main valley floor (Fig. 4A). Between these sites, the Hope fault is likely continuous but obscured by the active or recently active braid plain of the Taramakau River. The Kelly fault DDZ crosses the southern hillslopes with a morphologic expression characterized by low relief scarps on the perpendicular ridge tops (Fig. 4C marker 1), lineaments and fissures with a variety of orientations (Fig. 4A marker 2 and Fig. 4C marker 2). On the north side of the valley, Hope fault DDZ faults are expressed as sections of steepened hill slope (Fig. 4B) and shear zones revealed in landslide scars with little to no topographic expression. The Kelly fault DDZ faulting on the south side is more abundant than the Hope fault DDZ on the north side, but preservation may be enhanced by the lower slope hillsides on the south valley wall compared to the steeper north side. Within the river valley, intermittently exposed greywacke bedrock is often highly fractured and sheared to clay gouge (Fig. 6C). In the following paragraphs, we will describe the sites from east to west where we have completed detailed mapping around the Hope and Kelly fault PSZ traces.

At the easternmost extent of lidar coverage in the upper Taramakau valley (Fig. 4A and Fig. 5A), the Hope fault is expressed as a single trace striking $073 \pm 3^\circ$ that cuts two levels of fans on the north side of the valley. A channel on the lower fan surface follows the base of the riser between the two fan surfaces and has potentially modified the riser so it cannot be confidently used to measure lateral displacement, but the apparent strike-slip displacement is greater than apparent dip-slip displacement. Immediately east of the displaced fan surfaces, bedrock is exposed in the landslide scar on the north side of the river, exposing many fault surfaces including coarse gouge, and slickenlines in soft clay (Fig. 6A). One fault gouge zone strikes 080° , dips between 85° S to 85° N and projects toward the fault scarp on the upper fan surface (Fig. 6A). Along the same cliff face, 30 m further south, an outcrop exposes juxtaposed gravel in the hanging wall on the south side and bedrock in the footwall on the north side along a contact striking 070° and dipping 50° S (Fig. 6B). The gravel is poorly sorted, subrounded to subangular, gray, minimally weathered, with no visible sedimentary structure. The fault zone is 0.5 m wide, distinguished by where the gravel is distinctly more angular, with unweathered broken faces and more clay in the matrix but based on the lithology and size of the gravel clasts, it is the same original deposit as the unbroken gravel. The contact between the gravel and red bedrock does not have any striations or other slip indicators. Based on the crushed nature of the gravel, we interpret the contact between the gravel and bedrock as the edge of a fault zone, defined as the zone where the gravel is crushed.

In the same area in the upper Taramakau Valley (Fig. 5A), the Kelly fault PSZ is expressed as a single trace that strikes $065 \pm 5^\circ$ consisting of a break in slope along the hillside south of the Taramakau River. Highly

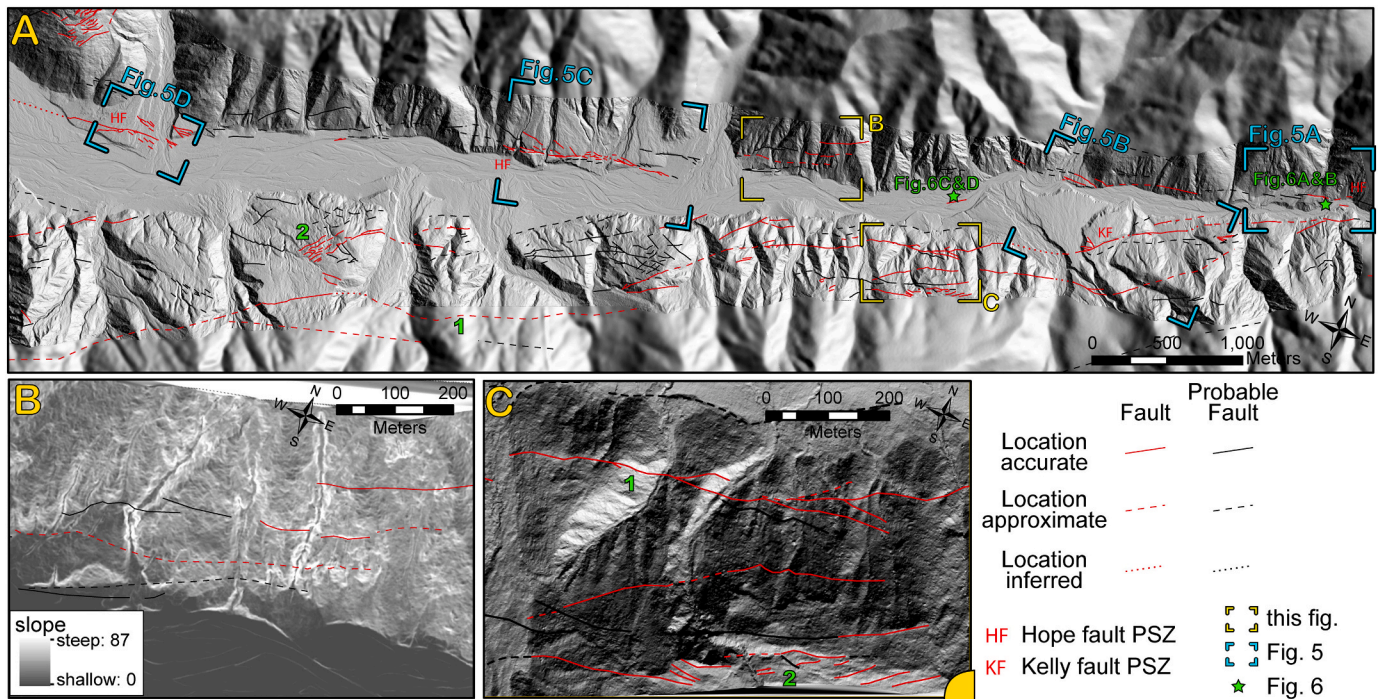


Fig. 4. A) Fault mapping in the upper Taramakau River valley. Extent is shown in Fig. 2. The green stars and labels indicate locations of field photos in Fig. 6. The extent for panels B and C are in yellow and extents for Fig. 5 maps are shown in blue. Green marker 1 shows the location of a prominent Kelly fault trace that is not covered by the lidar data. Marker 2 indicates part of the Kelly fault DDZ with a network of fissures. B) Slope map of the bare-earth lidar DEM and fault mapping on the north side of the Taramakau River valley depicting characteristic Hope fault DDZ traces delineated by downhill-facing scarps, which form linear sections of steep hillslope. In this section the Hope fault PSZ has no surface trace and is likely beneath the active river braid plain. C) Fault mapping on the southern side of the Taramakau River valley, showing a Kelly fault DDZ trace with low relief scarp (1), and network of small faults (2). The hillshade is from 135° (SE) azimuth, to highlight the uphill (south) facing scarps. (For interpretation of the references to colour in this figure legend, the reader is referred to the web version of this article.)

sheared fault rocks are exposed in a bedrock strath terrace remnant on the south side of the river, north of the geomorphic trace of the Kelly fault (Fig. 5A, marker 1). Riverbed outcrops ~2 km to the west also expose highly sheared fault rocks in a strath terrace (Fig. 6C and D, location in Fig. 4A). Although the Hope and Kelly faults have two distinct surface traces with evidence of accumulated multi-event displacement, the presence of highly sheared fault rocks between them indicate that there has been distributed deformation extending across the valley floor between the two mapped fault traces.

About 1 km west of the area in Fig. 5A, topographic data and detailed mapping near Locke Stream (Figs. 4A and 5B) indicate that the Kelly fault PSZ forms a north-side-up scarp that strikes $048 \pm 3^\circ$ and cuts alluvial/debris flow fans on the south side of the Taramakau River (classified as a Holocene post glacial fan by Barrell et al., 2011). The highest fan is dextrally displaced 91 ± 13 m with a H:V ratio of 26:1 based on matching of small, inactive channels on the fan surface (Fig. 5B offset KF1). The lower abandoned fan may also be faulted (Fig. 5B marker 1), but because the fan surface is nearly horizontal and the fault here is nearly pure strike-slip, any topographic surface expression of the fault is expected to be minimal; we found no unequivocal evidence to further support or refute this hypothesis. As there is no morphologic evidence on the lower fan for this fault or the splays that displace the higher fan, some or all of the apparent displacement of the western riser may be erosionally modified and not directly the result of fault displacement.

Roughly 3 km west of Locke Stream, Yeo Creek enters the Taramakau valley from the north, forming a variety of fan and terrace surfaces that are cut by the Hope fault PSZ (Figs. 4A and 5C). The fault cuts a low inactive terrace of Yeo Creek, where it has formed a 1 m high south-side-up (upstream facing) scarp striking $080 \pm 3^\circ$. A peaty bog has formed on the upstream side (Fig. 5C marker 1) with an unknown amount of sediment accumulation, so 1 m is considered a minimum scarp height. There are no features on the terrace surface that can be correlated across

the fault to determine lateral displacement. To the west, the fault crosses a group of large debris flow fans (Fig. 5C marker 2) that have been subsequently incised by streams, forming younger inset surfaces (Fig. 5C marker 3). On the south side of the fault trace the surface remnants are very small and do not contain distinctive markers so no reliable lateral displacement measurement can be made. The easternmost remnant could potentially be correlated with the eastern fans north of the fault, but it is not clear how much the western edge of the southern remnant has been modified by the stream flowing south.

About 3 km west of Yeo Creek, south flowing Michael Creek enters the Taramakau River from the north, forming a fan that is cut by the Hope fault (Figs. 4A and 5D). East of Michael Creek, the fault deforms a high fan surface via a branching set of north-side-up fault splays (Fig. 5D marker 1). There are traces of the fault on the second to lowest fluvial terrace, but not the lowest (Fig. 5D marker 2). On the Michael Creek fan west of the active stream channel, multiple levels of fan remnants and terraces are cut by the fault which strikes $080 \pm 5^\circ$ with dextral, south side up displacements ranging from 3.7–18.9 m right-lateral and maximum 2.4 m vertical separation. The displacement measurements are greater on the higher, older surfaces. The displacement of the fault here is south side up with a H:V ratio of 3.5 ± 1.5 at the location of the most confident displacement measurement (Fig. 5D marker HF1).

South of the Taramakau River, west of Locke Stream and east of the Oteha River valley (Fig. 5B) we have not identified any Kelly fault PSZ, but the DDZ widens, diverging toward the south away from the Taramakau River and the Hope fault PSZ (Fig. 4A and 7A and C). Some mapped fault traces have surface expression subparallel to the main Taramakau River valley consisting of small (1–2 m) uphill facing scarps or topographic benches (short section of flatter slope) on the ridges between small tributary streams (Fig. 4C marker 1). Where the scarps can be traced downslope into valley bottoms, the trace is generally further north than the scarp at higher elevations ('v's downstream'); if

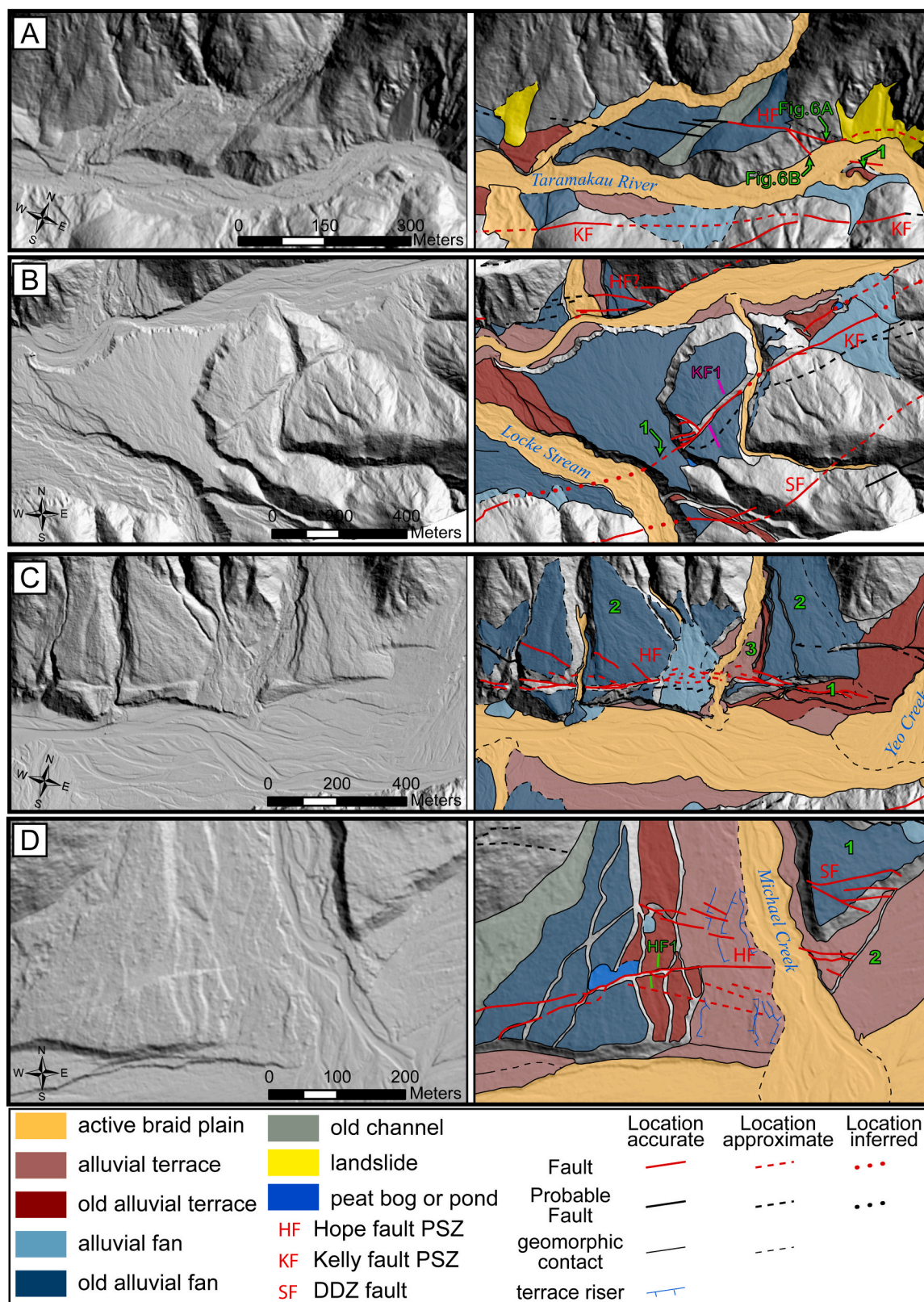


Fig. 5. Site maps with geomorphic and fault mapping from the upper Taramakau valley. Location of maps are indicated in Fig. 4 and details are discussed in the text. Green numbers indicate specific sites of interest referred to in the text. Hope fault PSZ (HF), Kelly fault PSZ (KF) and major secondary faults in the DDZ (SF) are indicated with red letters. A) eastern end of the lidar extent. B) Locke Stream fan cut by the Kelly fault PSZ. C) Yeo Creek and surrounding fans cut by the Hope fault PSZ. D) Michael Creek fan and incised terraces cut by the Hope fault PSZ. The most confident displacement measurement is identified in green as HF1. (For interpretation of the references to colour in this figure legend, the reader is referred to the web version of this article.)

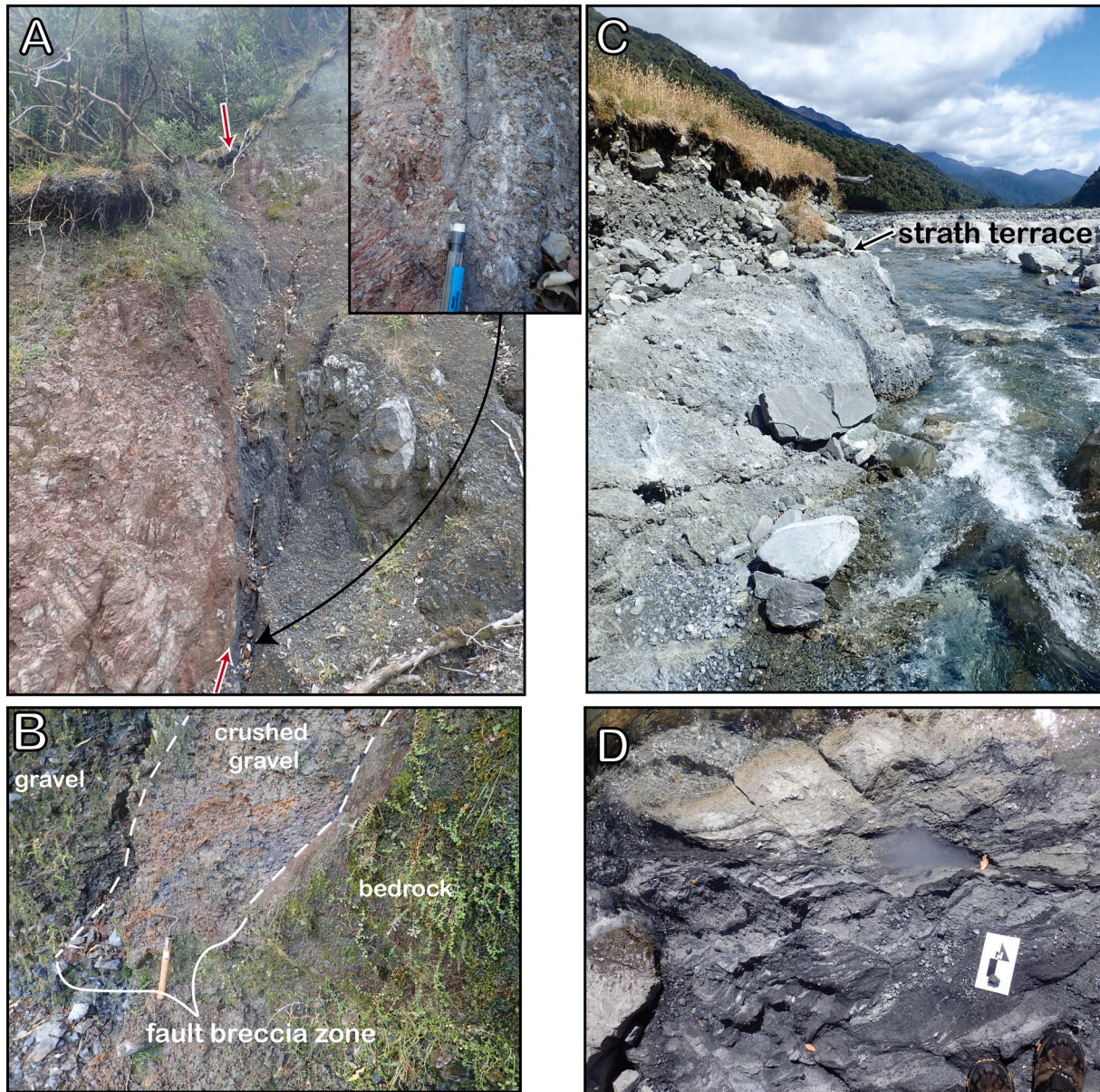


Fig. 6. Field photos of fault exposures in the upper Taramakau valley. Photo sites are indicated in Fig. 4. A) Photo location indicated in Fig. 5A, looking west. Fault gouge in a landslide/river cutbank exposure. Fault aligns with the geomorphic scarp in Fig. 5A. B) Photo location indicated in Fig. 5A, looking WNW. Fault juxtaposing gravel and bedrock. Within ~ 0.5 m of the bedrock surface the gravel is crushed and colored with soft interstitial clay deposits, defining the fault breccia zone. Gravel more than 0.5 m from the bedrock contact are coarse, poorly sorted, angular to subangular and slightly bedded. C and D) photos from within the active Taramakau River near Locke stream, indicated in Fig. 4A, A looking west, B looking down on the same outcrop. Fault gouge exposed in the Taramakau River channel and in a strath terrace ~ 1 m above the river level at the time of the photo (March 2019).

the fault is planar, these relationships indicate a dip of $70\text{--}80^\circ$ to the north and strike $063 \pm 5^\circ$. To the west the mid-elevation bench scarp becomes wider, forming low slope and low relief platforms on the ridges between tributary streams (Fig. 4A marker 2 and Fig. 4C marker 2). These low relief platforms are cut by the Kelly fault DDZ, expressed as arrays of discontinuous, low apparent displacement faults and fissures with a variety of strike orientations (Fig. 4A marker 2 and Fig. 4C marker 2). Some apparently significant traces of the Kelly fault occur off the south side of the lidar coverage (Fig. 4A marker 1). No reliable displacement measurements could be made between Locke stream and the Otehake River valley, due to a paucity of unambiguously offset correlative geomorphic features and lack of PSZ scarps with measurable displacement.

4.2. Hope fault in the lower Taramakau River valley

West of Michael Creek, the Taramakau River valley trends 080° to 100° (Figs. 2 and 7). Based on bedrock metamorphic zone offsets across the valley, the Hope fault was previously mapped in the Taramakau valley westward to meet the Alpine fault around Inchbonnie (Nathan et al., 2002). Alluvial fan and fluvial terrace surfaces examined using lidar and airphotos cumulatively cross the entire width of the Taramakau valley, so an active fault passing down the valley would have to cut one or more of these surfaces (Fig. 8). However, the high sediment yield and discharge within the lower Taramakau, with contributions from the Otira and Otehake rivers, may frequently refresh these fluvial and alluvial surfaces, especially following a large, surface rupture producing earthquake that will initiate extensive landsliding (e.g., Sheridan, 2014; Robinson et al., 2016; Massey et al., 2018). Determining if

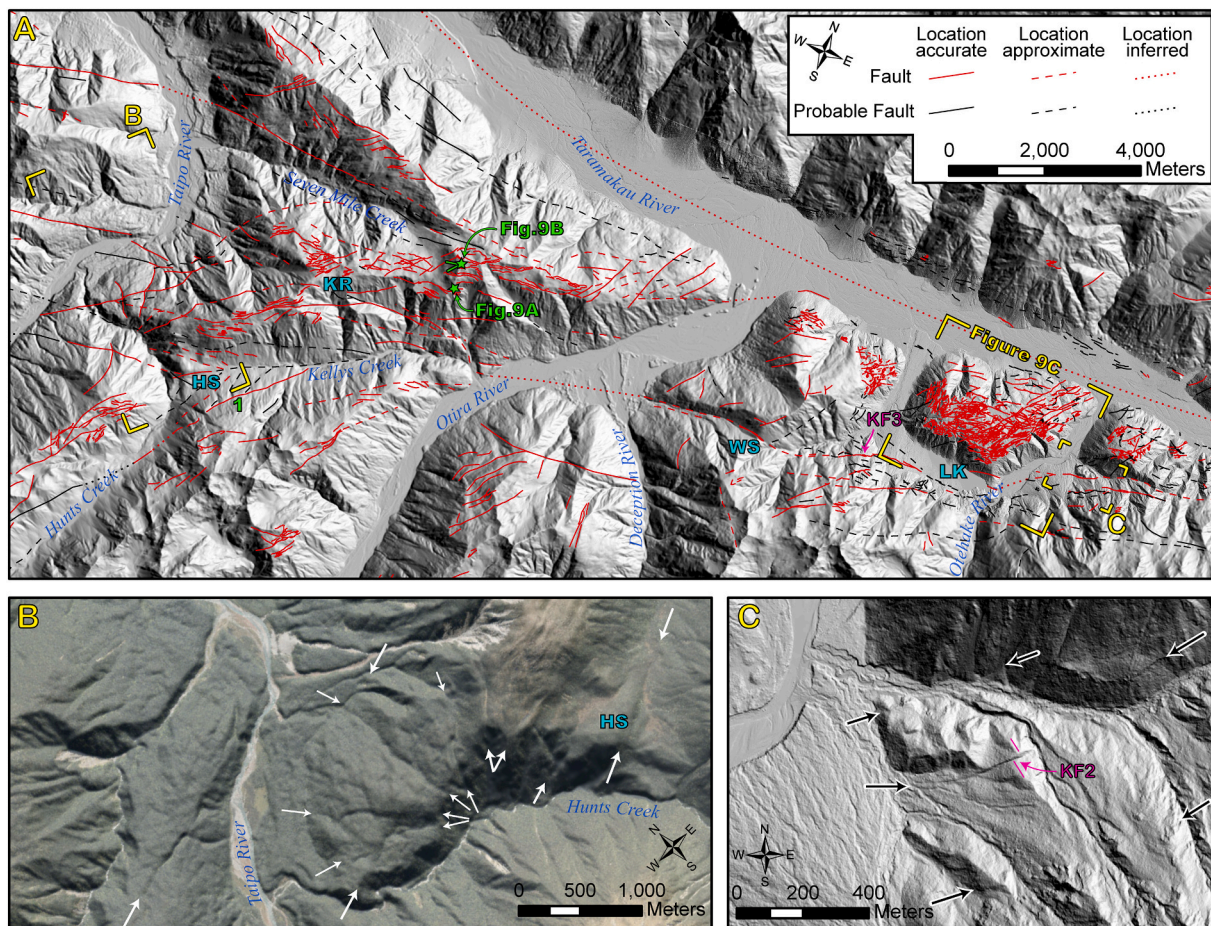


Fig. 7. A) Fault mapping in the central section of the study area. Rivers and creeks referenced in the text are labeled in blue. Significant geographic sites are labeled in cyan: HS – Hunt Saddle, KR – Kelly Range, LK – Lake Kaurapataka, WS – Waharoa Saddle. The location of Fig. 9A and the look angle (V) and photographer position of Fig. 9B are shown by the green stars. Displacement measurement KF3 is indicated in magenta. Extent of Fig. 9C and insets are shown in yellow. B) Airphoto and pDTM hillshade with arrows indicating faults. The Taipo River has apparent dextral offset that corresponds with a fault trace. C) Kelly fault main trace and some secondary traces indicated with arrows. Offset KF2 is marked in magenta. (For interpretation of the references to colour in this figure legend, the reader is referred to the web version of this article.)

these surfaces are refreshed would require using landform dating techniques to determine if the geomorphic surfaces are younger than the most recent Hope fault surface rupture identified on other sections of the fault system to the NE. Because of potential post-seismic modification and/or re-setting of these surfaces, a lack of direct fault evidence does not necessarily rule out an active fault within the valley, although the lack of surface expression does preclude determination of kinematics using the tools employed in this study. Using the pDSM, we have mapped some hillside lineaments in the lower Taramakau valley as probable faults (Fig. 7). These features are discontinuous with low apparent displacement, similar to the secondary faults upstream (Fig. 4B and C), so we do not interpret them as a significant tectonic fault. The lidar at Inchbonnie also does not reveal any features that can be uniquely attributed to the Hope fault based on slip kinematics and/or alignment with the Taramakau River valley.

Some geomorphic features within the lower Taramakau valley suggest the presence of an active fault striking along the valley axis, with a south side down component of displacement. Ultimately, the Alexander Range to the north of the river is an average ~ 300 m higher and with peaks ~ 500 m higher in elevation than the Bald and Kelly ranges south of the Taramakau River (Fig. 2). There are also some more specific geomorphic indicators suggesting a south side down Western Hope fault. For example, Barrell et al. (2011) mapped an ice-carved bench on the south side of the valley that is 100–200 m lower elevation than the outlets of hanging valleys directly across on the north side of the valley,

this elevation difference may indicate that the north side has uplifted relative to the south side since the LGM. The long profile of streams on the south side of the valley are consistently smooth and concave, while the northern streams have a convex profile characteristic of both hanging valleys and actively uplifting range fronts. The local range front, where alluvial fans meet bedrock slope, is more sinuous on the south side of the valley than on the north. This metric has been used on larger range fronts to infer tectonic activity and relative uplift rate, where the faster uplifting range front has a more linear and less sinuous range front than slower uplift terranes (Burbank and Anderson, 2011). The north side of the valley is overall much steeper than the southern slopes and exhibits almost faceted morphology. The combination of all these features offers tentative support for our hypothesis of an active, south side down fault (Western Hope Fault) within the Taramakau valley.

4.3. Kelly Fault between Otehake River and Otira River

Between the Otehake River and the Otira River, the Kelly fault PSZ continues to diverge from the Taramakau River valley (Fig. 7). The Kelly fault PSZ is mapped on the hills east of the Otehake river (Fig. 7C), and it cuts the fans and hillsides west of Lake Kaurapataka (Fig. 7A “LK”) up to Waharoa saddle (Fig. 7A “WS”) where the fault trace is apparent beneath the sub-alpine bush. Despite field investigation, pDSM and airphoto analysis, we have found no trace of the Kelly fault on the Deception

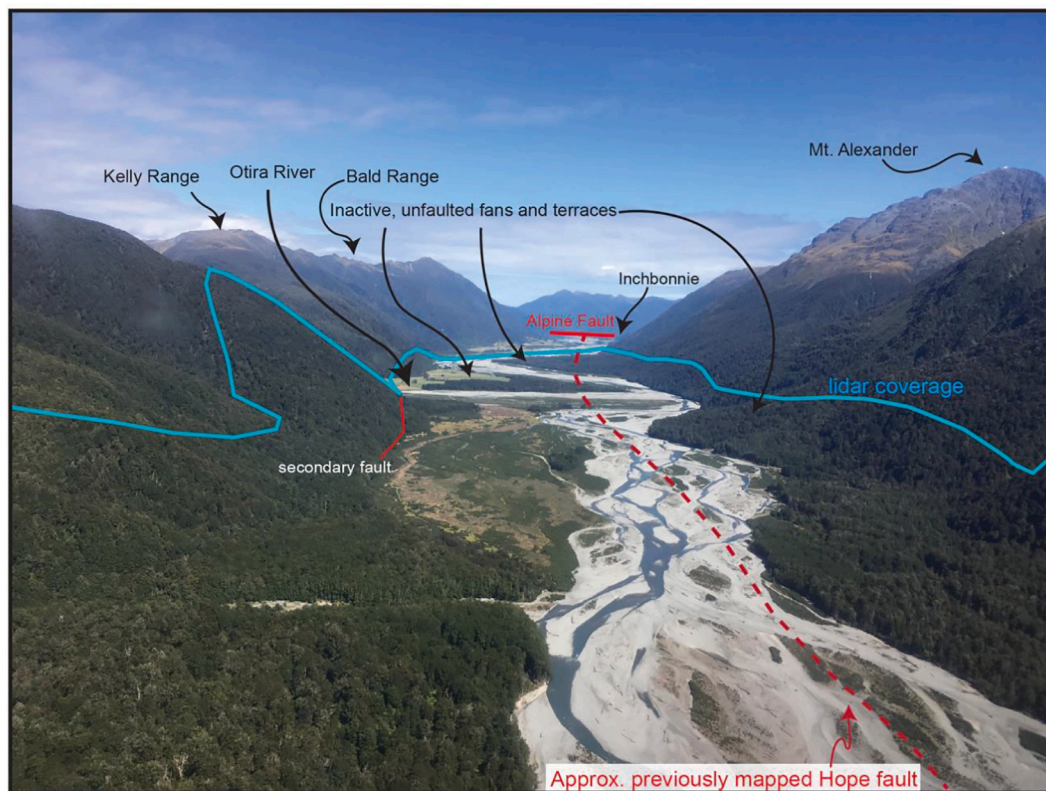


Fig. 8. Annotated oblique aerial view of the lower Taramakau valley, view to west. Photo position, look direction, and geographic sites are indicated on Fig. 2B. In the distance, the Alpine fault crosses the Taramakau River at Inchbonnie. Lidar coverage is shown by the blue line and extends across the valley and up the lower $\sim 1/3$ of the valley walls. Vegetated, inactive fan and terrace surfaces collectively extend across the valley floor and do not show geomorphic evidence of an active fault trace. The potential trace location for the Hope fault is shown, demonstrating that even if it were shifted to the north or south, it would cross presently inactive fans that have lidar coverage. (For interpretation of the references to colour in this figure legend, the reader is referred to the web version of this article.)

River fan along strike from the Kelly fault PSZ on Waharoa saddle. Recent aggradation on the Deception River fan has likely buried the active trace of the Kelly fault across the fan surface. At offset KF2 (Fig. 7C), a low ridgeline is displaced dextrally by 16 ± 6 m, and 7 ± 0.5 m vertically, yielding a H:V ratio of 1.3:1 to 3.8:1. At offset KF3 (Fig. 3B and 7A) a small channel with a similar trend on either side of the fault and similar cross-sectional shape is dextrally displaced 91 m ($+21.4$, -12.4) and vertically offset between 2.5 and 5 m, with a H:V ratio ranging from 18:1 to 36:1. The large range on this displacement measurement is because a small fan-like accumulation of sediment against the uphill facing fault scarp obscures the channel within ~ 40 m of the fault scarp. At KF2 and KF3, the PSZ has apparent strike $070 \pm 5^\circ$, but the fault at Waharoa saddle has apparent strike $\sim 090^\circ$. Along this section, faults within the Kelly fault DDZ are subparallel to the PSZ, with varied continuity and low apparent displacement. Distributed slip on these less developed faults may account for the total displacement discrepancy between KF2 and KF3, as they share an unknown portion of the total fault slip.

4.4. Gravitational faulting

We have identified fault networks that are mostly limited to the upper $1/3$ of the elevations in the regional topography. Parallel fault sets occur on a single slope and do not cross the summit ridge crest (Fig. 9A). They dip into the mountain and have normal slip, creating uphill facing scarps, they strike roughly perpendicular to the steepest slope direction, are short in length relative to their apparent dip-slip displacement, and have a slightly arcuate trace (Fig. 9A). Faults like these have been noted in many mountainous landscapes, with some variations in exact morphology and process, leading to a variety of names (sackungen,

ridge rents, antiscarps or antislope scarps) but all are considered to be driven primarily by gravitational processes acting on topography (Zischinsky, 1969; Beck, 1968; Lensen, 1976; Pere, 2009).

Networks of cross-cutting faults occur on the flat-topped hills between the Kelly fault PSZ and the Taramakau River, including but not limited to, parts of the Kelly Range and the hill between Lake Kaurapataka and the Taramakau River, which we informally name Sackung Hill (Fig. 9B and C). These fault networks are different from typical antiscarps in that they have a variety of strike directions that are mutually crosscutting and do not necessarily strike perpendicular to the local steepest slope. They generally dip toward the center of the mountain and have apparent normal kinematics. On the Kelly Range, these faults have been studied previously and attributed to gravitational adjustment of glacially over steepened ranges subjected to repeated large magnitude earthquakes (Fig. 9B) (Beck, 1968; Pere, 2009).

The use of lidar enables us to map in great detail a network of mostly previously unidentified faults beneath dense vegetation cover on Sackung Hill in great detail (Fig. 9C and D). The surface of the hill is covered with glacial striations that are cut by the faults and provide a datum for measuring fault offsets and kinematics. The faulting appears to be entirely post-glacial because there is no glacial deposition on down-thrown sides or much degradation of the upthrown side, and the striations do not appear to exhibit any systematic variations in trend, amplitude, or other physical attributes that would indicate they were formed across pre-existing fault topography. Because the striations are at a high angle to, and cleanly cut by, the faults they provide useful markers of fault kinematics.

The faults have a hierarchical (fractal) frequency - length relationship (Fig. 9E) with similar statistical properties to a Gutenberg-Richter distribution for seismicity (Gutenberg and Richter, 1944; Rundle,

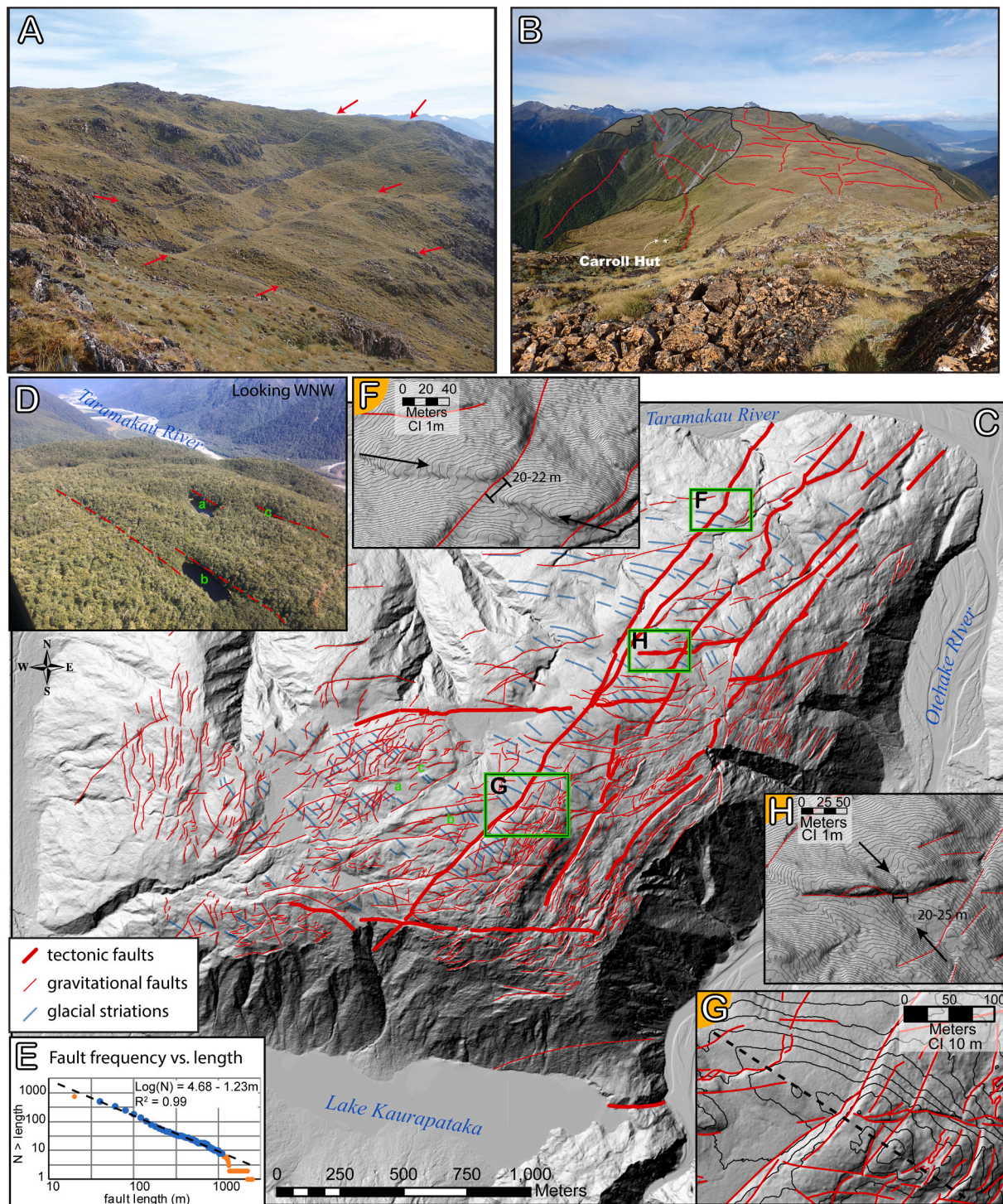


Fig. 9. Gravitational faulting A) Anticarsps on the Kelly Range, faults are indicated by the red arrows. The photo location is indicated on Fig. 7A, photo is looking north. B) Annotated photo of the fault network on the Kelly range. Photographer location and look direction (roughly southwest) indicated on Fig. 7A. C) Map of the faults and glacial striations on Sackung Hill between Lake Kaurapataka, Oteha River, and Taramakau River, extent indicated on Fig. 7A. D) Helicopter oblique photo of the top of Sackung Hill, looking west. Fault bounded ponds and peat bogs occur on the top of the 800 m high hill. Ponds are labeled in photo and in map C for orientation. Only the largest fault scarps are identifiable beneath the dense forest cover. E) Fault frequency-length indicates a hierarchical relation of the fracture network. F, G and H) Site maps showing displacements on likely tectonic faults. Arrows indicate the landform being offset, and the displacement is indicated by the black barred line along the fault. In G, the dashed line indicates the trend of the crest of the glacial striation, which is not laterally displaced by the faults. (For interpretation of the references to colour in this figure legend, the reader is referred to the web version of this article.)

1989; Wesnousky, 1999; Öncel et al., 2001; Rundle et al., 2004). The majority of faults on the hill are short (<100 m), discontinuous, and have normal displacements, indicating they may have a gravitational origin with kinematics driven by topographic instability and distortions

of the stress field through earthquake loading (Li et al., 2010; Kinakin and Stead, 2005; Savage and Varnes, 1987). We recognize two sets of active tectonic faults, NNW-striking and EW-striking, both have characteristics unusual for gravitational faults including crossing the ridge

crest, they are linear rather than arcuate, extend into lower elevation areas, and have dextral displacements (Pere, 2009; Khajavi et al., 2014). The NNE-striking faults have dextral displacements at low elevations (Fig. 9E) and normal displacements at high elevations (Fig. 9F). This rake change is interpreted to be the result of interaction with the network of normal (sackung) faults at high elevations. The EW-striking faults also have dextral displacements (Fig. 9G). The dextral displacements on individual faults in both sets are 10 to 30 m, indicating they have accumulated slip from multiple surface rupturing earthquakes since deglaciation post-latest Pleistocene times. The two sets cross-cut each other, indicating they are coeval. We consider these tectonic faults to be part of the Kelly fault DDZ and interpret their structural significance as a relay structure transferring dextral slip from the Hope fault at Michaels Creek (Fig. 5D) to the Kelly fault PSZ south of Sackung Hill (Fig. 7, offsets KF2 and KF3).

4.5. Otira River valley to Alpine fault

We have not identified any faulting within the Otira River valley, though the river is highly dynamic, so it likely refreshes the landforms frequently. Faulting within the Kelly's Creek valley is evidenced by the presence of exposed fault rocks (Freund, 1971; Nathan et al., 2002), although no fault trace can be identified with the current photogrammetric dataset. The Kelly's Creek valley is dominated by debris flow fans coming from both sides that are active and probably have obscured or buried scarps (Fig. 7A). There is a prominent fault scarp on the slope south of Kelly's Creek (Fig. 7A marker 1), that has been previously identified and mapped as the Hunt Creek fault (Fig. 2A) (Nathan et al., 2002; Berryman et al., 2003; Langridge et al., 2016). This fault does not obviously link up with any other fault traces, but we have mapped disorganized fault scarps in Hunt Saddle and on the south end of the Kelly Range that may link the Hunt Creek fault with the faults to the west (Fig. 7B).

West of the Kelly Range, the number of mapped fault traces increases as the Western Kelly DDZ approaches the Alpine fault and splays form between them. In this area, where lidar coverage is limited to Alpine fault swaths and the Styx River valley, we use the pDSM and airphotos to identify abundant faults that have modal apparent strike of $090^\circ \pm 10^\circ$, with apparent dips both north and south and a variety of apparent kinematics (Fig. 10A). At least two significant dextral faults cross the Taipo river valley, evidenced as sections of the river that flow through canyons (as opposed to the intervening wide, flat valley bottoms) that deflect the river dextrally (Fig. 7B and Fig. 10A - markers 1 and 2). Further downstream, on the north side of Seven Mile Creek (Fig. 10A - marker 3) another fault crosses the Taipo River. Although this fault may cut some large fluvial terraces, the fault cannot be accurately mapped on these terraces with the pDSM. On the hill slopes, it is identifiable by a bench scarp that has apparent strike $095 \pm 3^\circ$ (Fig. 10A marker 3). We have identified another trace along strike that appears to intersect the Alpine fault trace, but the details of the intersection cannot be observed in the pDSM or airphoto (Fig. 10B). Other fault traces mapped in between the Taipo River and Alpine fault are discontinuous, we attribute this to the limitations of the dataset since only large scarp features can be identified on the pDSM. The watershed scale geomorphology of this area seems to be relatively unaffected by the faults and is not dominated by fault parallel rivers, but by radial drainage pattern of the Tara Tama Range (Fig. 10A). This affects the appearance of faulting, making the surface expression variable due to complex interactions with topography (Fig. 10C). However, this also allows us to make strike and dip measurements of some of these fault splays using rule of V's. Many of these faults have apparent dextral-normal displacement, but with the pDSM we are unable to make precise kinematic measurements because we cannot truly match correlative features across the fault. However, despite the various orientations of topography, the fault traces mapped here dominantly have apparent strike of $090 \pm 10^\circ$, $\sim 20^\circ$ divergent from the strike of the Kelly fault PSZ identified east of the Waharoa

Saddle (Fig. 7).

The lower Taipo, Arahura, and Styx River valleys are wide, glacial valleys filled with large volumes of post-glacial alluvium and alluvial fans (Nathan et al., 2002; Barrell et al., 2011). Where the Taipo River approaches and crosses the Alpine fault, it passes through a steep canyon where the fault has uplifted post-last glacial terraces (Fig. 10A - marker 4). The lidar strip map along the Alpine fault here does not reveal any trace of an incoming Kelly fault splay; the faulting and folding can be attributed to the Alpine fault. Cutbanks on the Arahura River reveal Alpine fault exposures at the range front that dip $\sim 30^\circ$ east (Rattenbury, 1987). The Styx River is a short river that extends only ~ 12 km into the Southern Alps and the watershed does not reach the Main Divide. It has a wide valley full of high, deeply incised postglacial fans, and there is no canyon where the river crosses the Alpine fault (Fig. 11). Lidar in the Styx River valley reveals there is only a single mappable fault trace crossing the alluvial fans on the south side of the valley (Fig. 11), consistent with the previously mapped Hura fault, a splay of the Kelly fault (Nathan et al., 2002). The fault scarp on the fan surfaces strikes $095 \pm 5^\circ$ has ~ 5 m of vertical displacement, creating a bench on the steep fan surface (Fig. 11 - marker 1). Where the fault crosses perpendicular features like stream channels there is no lateral offset recorded. At the fault, the deeper channels have knickpoints but the shallow channels do not. The deeper channels may have reached down to bedrock, facilitating knickpoint preservation after fault displacement, but the shallower channels may still be within alluvial material where creek bed displacements are quickly eroded after surface rupture.

Approximately 2 km from the Alpine fault, the fault trace crosses bedrock hillsides, continuing linearly from the trace on the Styx River valley fans (Fig. 11 - marker 2). Here there are many knickpoints in the stream channels, but few other geomorphic markers. The range front has a small saddle where this fault crosses and extends toward the Alpine fault (Fig. 11 - marker 3). This fault then meets the Alpine fault in a pop-up that deforms the alluvial fan between the Styx and Kokatahi Rivers (Fig. 12) (Langridge et al., 2020). At the fault intersection, the Alpine fault has a ~ 300 m left step, which appears to be the principal cause of formation for the pop-up structure. The pop-up deforms a post-glacial fan surface, and streams coming off the saddle (Fig. 11 - marker 3) have incised through the deformed alluvial material. The fan surface appears to be intact across the faults aside from the deep, narrow incised channels. An Alpine fault parallel topographic profile across the pop-up (Fig. 12A) shows a smooth decrease in height from ~ 190 m elevation at the peak of the pop-up across the remnants of the fan surfaces to the north where the remnant surfaces level off at ~ 120 m elevation. Although there is a complex network of faults across the whole intersection, most of the vertical deformation appears to occur south of the most prominent Kelly fault splay across the northern edge of the fan. The southern, less prominent, Kelly fault splay extending west from the small rangefront saddle would intersect south of the highest part of the pop-up. The flat surfaces within the fault intersection area (Fig. 12A - marker 1) are lower than the main fan surface. It is unclear if these surfaces are coeval with the upper surface and down-dropped by complex faulting, or if they are younger surfaces formed by erosion during different stages of fluvial incision; age dating of the surfaces would be required to distinguish the two formation mechanisms. This example of young, active intersection and mutual crosscutting of the Kelly and Alpine faults traces indicates the faults are coeval, physically intersect, and actively transfer slip, likely within single earthquake ruptures.

5. 3D fault model

5.1. Methods

To understand the geometry and kinematics of the fault system beyond the mapped surface faulting, we constructed a 3D virtual fault model with Leapfrog Geo© and used slip vector balancing to infer the kinematics where they could not be measured directly from surface

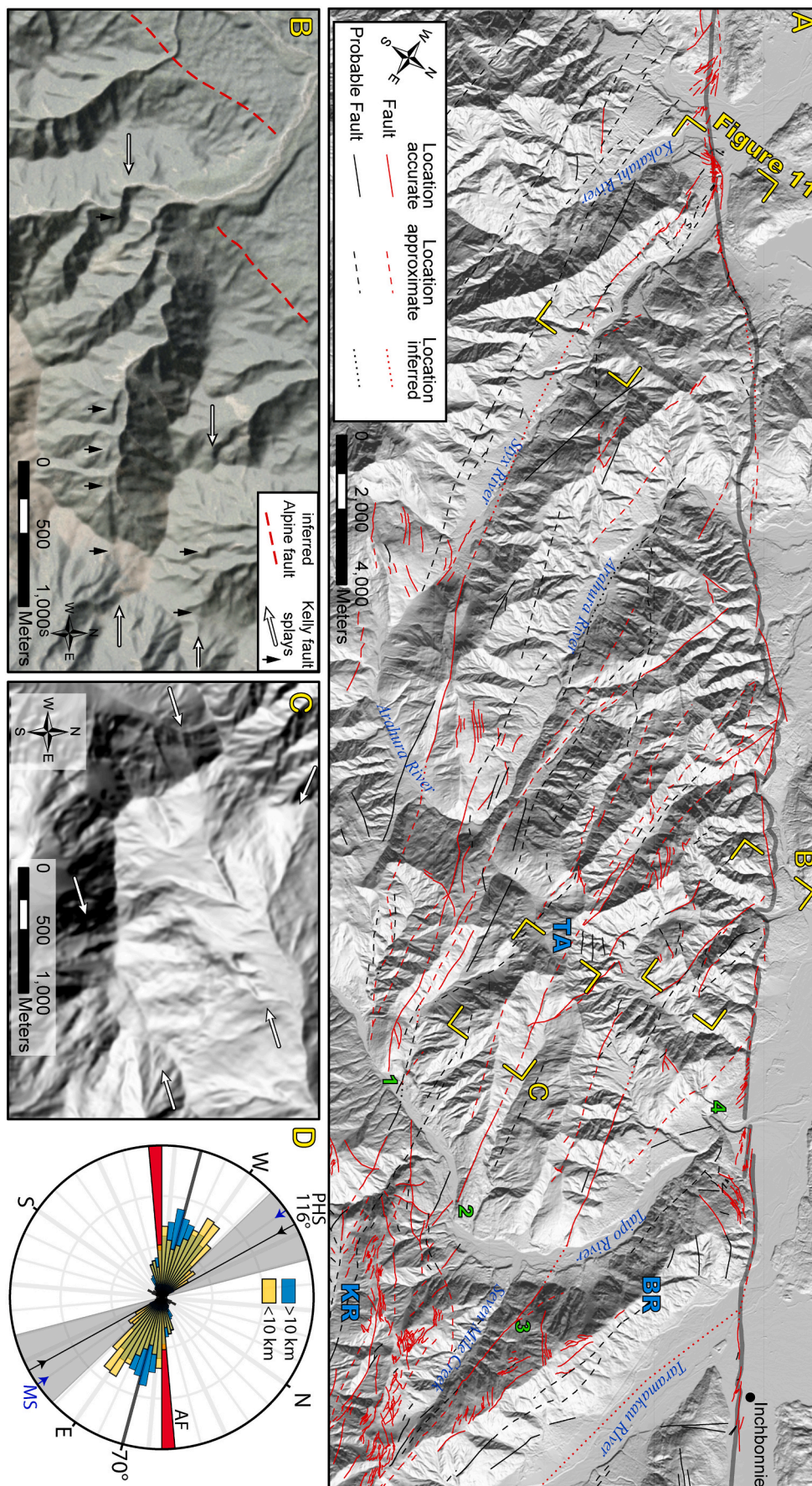


Fig. 10. A) Map showing faults within ~10 km of the Alpine fault. Map orientation is indicated by the north arrow in the legend. Alpine fault trace from previous work shown by dark gray line (Nathan et al., 2002; Langridge et al., 2016). Extent of insets and Fig. 11 are shown by the yellow corner marks. Green number markers indicate locations referred to in the text. Geographic names are indicated in blue: TA – Tara Tama Range, BR – Bald Range, KR – Kelly Range. B) Map with pDSM hillshade over airphoto showing a splay of the Kelly fault (white/black arrows) approaching the Alpine fault (red dashed line). The Alpine fault in this section is serially partitioned, creating an apparently discontinuous trace with the available data resolution. C) pDSM hillshade showing an example of faulting within the ranges, with multiple fault traces crossing topography indicated by the arrows. D) Rose diagram rotated to the same orientation as A. The Alpine fault, principal horizontal stress direction (PHS) (Michailos et al., 2020), direction of maximum shortening (MS) (Haines and Wallace, 2020), and relative plate vector (070°) (Altamimi et al., 2016) are all shown. The fault trace trend, approximating strike, of faults mapped in this study are shown as rose diagrams. Faults greater than 10 km from the Alpine fault (blue) have modal trace trend (\sim strike) of $\sim 070^\circ$ and faults within 10 km of the Alpine fault (yellow) have modal trace trend (\sim strike) of $\sim 090^\circ$. (For interpretation of the references to colour in this figure legend, the reader is referred to the web version of this article.)

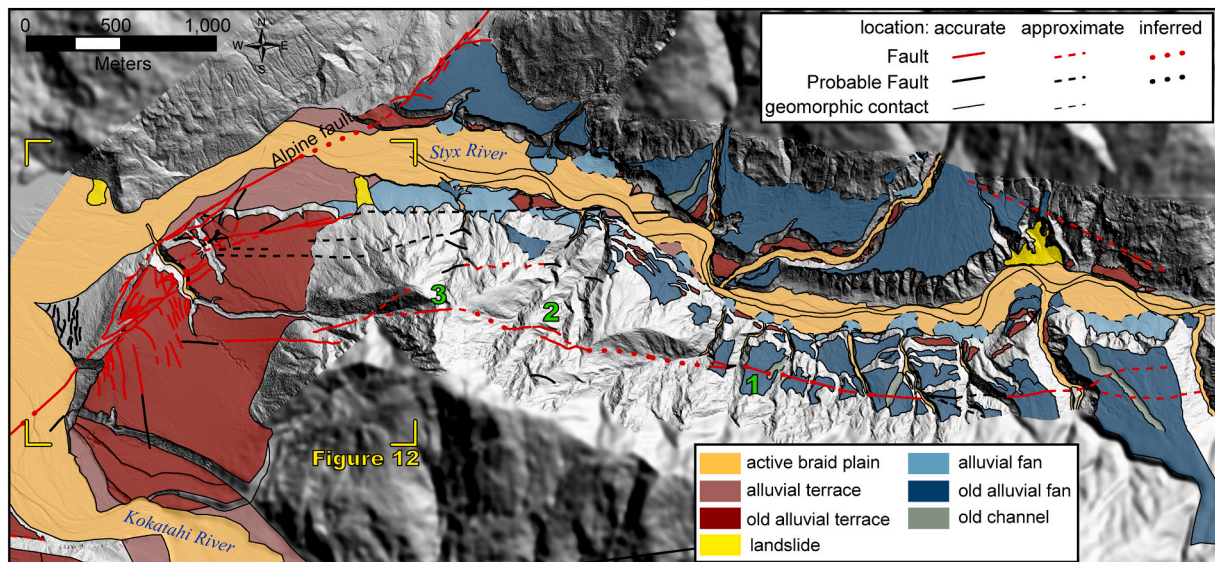


Fig. 11. Fault and geomorphic mapping in the Styx River valley, where the previously identified Hura splay of the Kelly fault meets the Alpine fault. Lidar coverage of this area enables detailed mapping. Green numbers indicate sites of interest discussed in the text. Extent of Fig. 12 is shown by yellow corner marks. (For interpretation of the references to colour in this figure legend, the reader is referred to the web version of this article.)

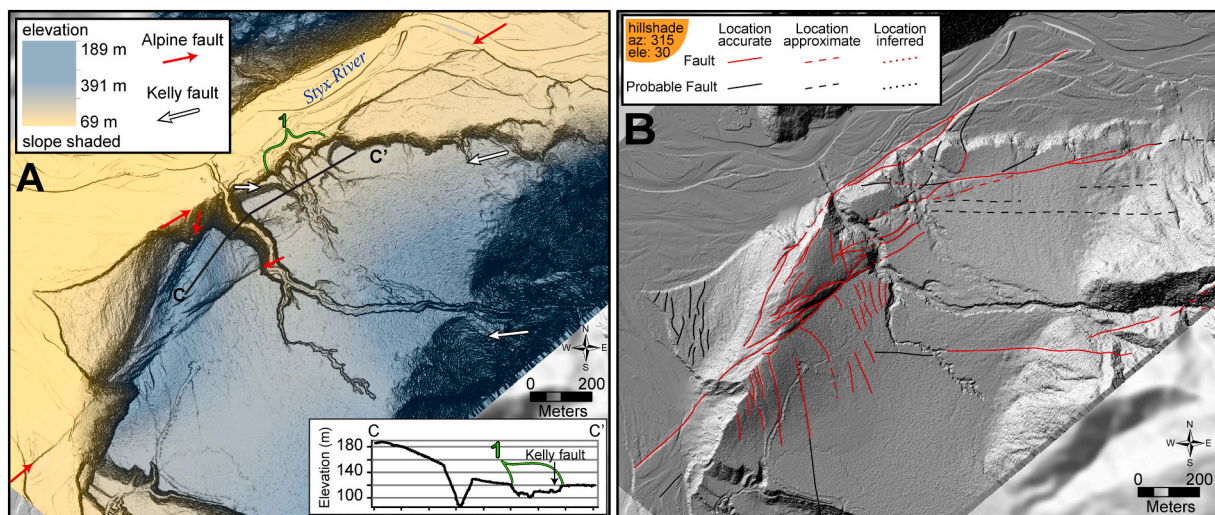


Fig. 12. Two maps of the fault structures at the junction between the Alpine Fault and the Hura splay of the Kelly Fault at the Styx River. A) Elevation on slope shade, where steep slopes are dark and flat areas are light. Main traces of the Alpine fault are indicated with red arrows, and the Kelly fault is indicated with white/black arrows. The Kelly fault has two incoming traces, but the northern trace has more displacement and is considered the main splay in this area. The inset profile runs from C – C' and is $\sim 2\times$ vertically exaggerated; the position of the Kelly fault main trace is indicated. B) Detailed fault mapping overlain on a low angle hillshade illuminated from 315° (NW). (For interpretation of the references to colour in this figure legend, the reader is referred to the web version of this article.)

displacements or outcrops. When creating the model, we aimed to minimize deviation from the observations and to minimize space problems while using the assumption of rigid block motions. We allowed for listric or curved fault planes, as warranted by the observations, but otherwise assumed planar faults. Fault locations and strike are based on mapped traces. For the model we simplified the dense network of discontinuous faults, especially in the western 10–15 km, by choosing the most continuous and highest confidence faults to use in the model. Where the mapped fault traces are discontinuous, we infer that along strike segments mapped with high confidence are part of the same fault plane. Where possible, we calculated the fault dip where the fault trace can be followed crossing topography using the rule of Vs (fault dips toward the location of the trace at lower elevations, dip calculated as a three-point problem). Where the fault dip could be determined at the surface, we simply inferred that this dip continued into the subsurface.

In the western 10–15 km of the study area, where the data are primarily from the pDSM, precise dip determinations were not possible. Because the faults in this area abut the Alpine fault within the brittle crust and are the first link in the slip transfer onto the Hope fault, we assume relative neutral intersections and rigid blocks and use slip vector balancing to determine likely dip and kinematics for these faults given the mapped strike range.

A neutral fault intersection is one where the slip vectors of both faults are parallel to the intersection line between the two faults (Fig. 13A); this strain-efficient intersection geometry minimizes necessary block volume changes. To determine if two faults could have a neutral intersection, we create a stereonet plot with the fault orientations as planes and known slip vectors as rakes on those planes (Fig. 13B). Known slip vectors are determined from either published slip-rate ratios (strike-slip to dip-slip rates, Fig. 13E) or H:V displacements as measured in this

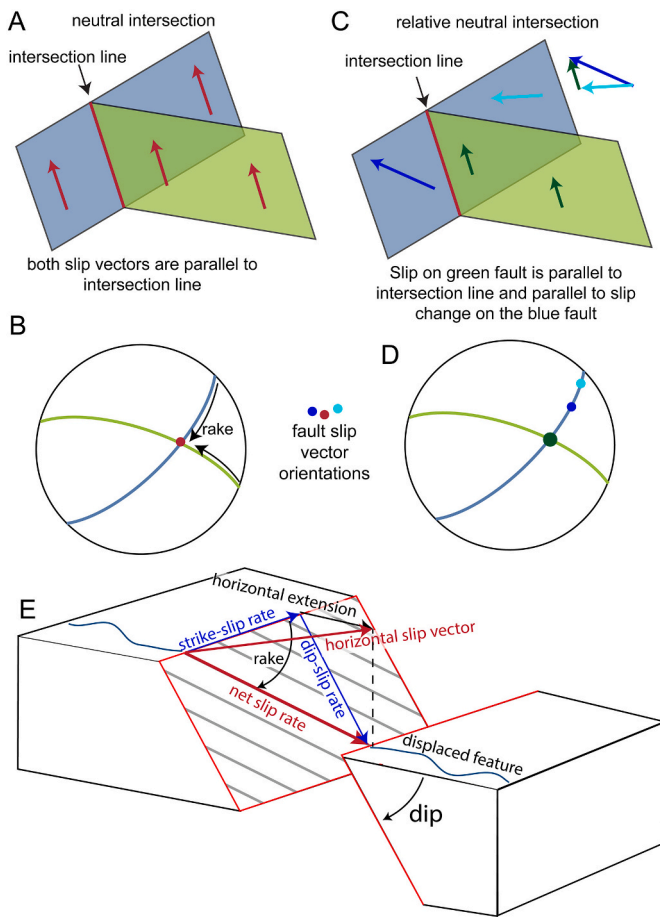


Fig. 13. Slip vectors, neutral intersections, and fault geometry. A) 3D fault schematic showing a dominant fault (blue) and an abutting subordinate fault (green) with parallel slip vectors and a true neutral intersection because the intersection line is parallel to the slip vectors. B) Stereonet plot of the faults and slip vectors in A. The intersection of the two fault planes and the slip vectors are aligned and represented by the red dot. C) 3D schematic of two faults with a relative neutral intersection. The slip vectors of the dominant fault (blue fault, blue and light blue vectors) change across the intersection. The fault intersection line (red) and the slip vector of the abutting subordinate fault (green) are parallel to the slip deficit of the dominant fault. D) Stereographic representation of the faults in C. The fault planes are plotted, and the slip vectors are shown in the same colors as the vectors in B. The slip vector of the abutting fault is parallel to the intersection, but not the slip vectors of the dominant fault. E) Block diagram of an oblique fault showing the various measures of fault orientation and slip directions used in this paper. (For interpretation of the references to colour in this figure legend, the reader is referred to the web version of this article.)

study. If the slip vectors of two intersecting faults overlap at the intersection point, then the faults have a neutral intersection (Fig. 13B). In cases where the dominant fault changes slip rate across the intersection (Fig. 13C) and the slip deficit is accommodated by or transferred onto the abutting fault, a relative neutral intersection may exist. In a relative neutral intersection, the slip vectors of the dominant fault may not be parallel to the fault intersection line, but if the intersection line is parallel to the vector of the slip deficit on the dominant fault, the missing slip can be transferred directly onto the abutting fault. The slip vector of the abutting fault will be parallel to the intersection line, if the rigid block assumption is true, because block movement requires slip along both fault planes. If the slip vector of only one fault is known, we can estimate a compatible orientation and/or slip vector for the second fault to create a neutral intersection or relative neutral intersection. By assuming rigid block deformation, we can estimate dip and kinematics

for faults of unknown orientation at or near the intersection by determining the range of values that can accommodate the slip differential via relative neutral intersections. We use a combination of a simplified fault geometry where splays are represented by an average fault plane, stereonets to determine fault plane intersection orientations, and known fault slip-rate values plotted in horizontal vector space to determine the slip that needs to be accommodated through the intersection and the possible fault geometries that can do it.

5.2. 3D model results

The mapping provides direct constraints for the position, orientation and kinematics of the Hope and Kelly faults in the Taramakau River valley upstream of the Otira River where lidar coverage allows detailed fault trace mapping. Based on the mapping, we have modeled the Hope and Kelly faults as distinct structures on the north and south side of the valley, respectively. Because of the $\sim 70^\circ$ N dip of the Kelly fault, and nearly vertical dip of the Hope fault, they likely converge within the upper 5 km, this is reflected in the model (Fig. 14). We included a representative NNE-striking connecting fault through Sackung Hill in the model (Fig. 14), though the mapping suggests there are more similar faults spanning between the Hope and Kelly faults. In the western 10–15 km of the study area we simplify the dense fault network (Fig. 10) and model the Western Kelly fault DDZ as 5 splays in a horseshoe arrangement (Fig. 14). This is undoubtedly a simplification of the fault system, but because the majority of the mapped faults have similar strikes (i.e. there is not an abundance of cross-faults, but many sub-parallel faults with various displacement magnitudes, see Figure 10D) we consider the 5 splay simplification a reasonable representation of the system while being sufficiently simplified to model. Mapped Western Kelly fault splays about the Alpine fault at the surface, based on observations of direct fault interaction at the Styx River site (Section 4.5, Fig. 12), and this abutting relation is likely also true within seismogenic depths. The mapping does not provide confident constraints on the dip or kinematics of the faults in the western 10–15 km. Since we know the net slip rate change of the Alpine fault across the intersection (Norris and Cooper, 2001; Langridge et al., 2010), and the strike of the Western Hope fault and Western Kelly fault splays, we use slip vector balancing and the assumptions of relative neutral intersections and rigid blocks to constrain the potential dip and kinematics of the Western Hope fault and Western Kelly splays in this section.

For the slip vector balancing, we must set up the slip circuit we want to solve, starting by defining a simplified model of the faults and intervening blocks (Fig. 15A). We simplify the Western Kelly fault DDZ as one fault since most of the fault splays have similar apparent strike. We consider the Western Hope fault as a separate structure from the Western Kelly fault DDZ, because it has more apparent bedrock displacement, a more developed large scale geomorphic signature (the wide Taramakau River valley) but no localized surface expression. This results in four faults: central Alpine fault, northern Alpine fault, Western Hope fault (WHF), and Western Kelly fault DDZ (WKF). These faults bound the four blocks: a (west of the Alpine fault), b (east of northern Alpine fault and north of WHF), b2 (east of Alpine fault, south of WHF and north of WKF), and c (east of central Alpine fault, and south of WKF). For the model, each of these faults is considered to have slip that accommodates the entire relative horizontal velocity between the blocks on either side. The strike-slip and dip-slip rates on the Alpine fault at Inchbonnie and Kakapotahi are known (Langridge et al., 2010), and previous work indicates possible dips as steep as 60° (Langridge et al., 2010; Carpentier et al., 2013) to as shallow as 30° (Rattenbury, 1987; Barth et al., 2013; Nathan et al., 2002; Rattenbury and Vidanovich, 2018). We assume 50° SE dip for the Alpine fault and calculate the horizontal slip vector at Inchbonnie and Kakapotahi (which is also the relative velocity between the blocks at each site) by converting the dip-slip rate into horizontal shortening and combining that with the strike-slip rate, resulting in a horizontal slip vector that trends slightly more E-

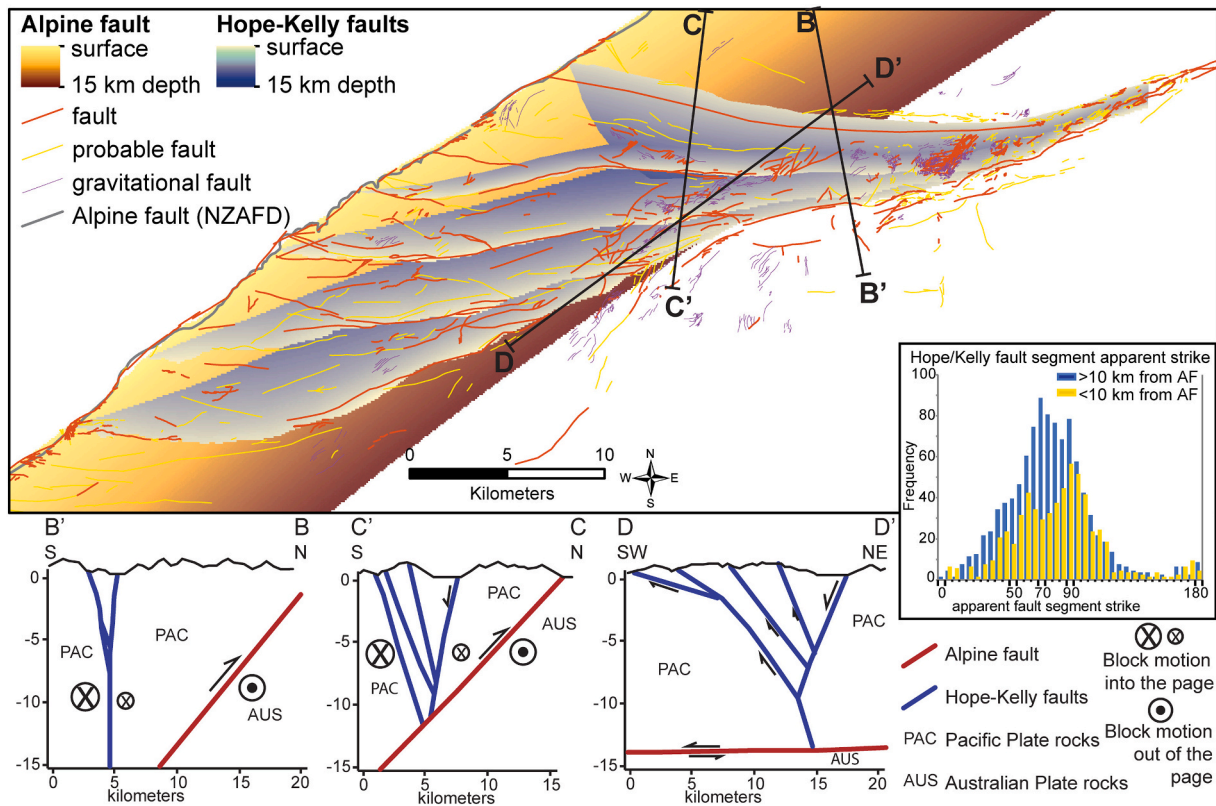


Fig. 14. Map and cross sections of the 3D virtual fault model. A) Map of the Hope-Kelly fault system and modeled fault planes. The surface trace of the modeled fault planes corresponds to aligned, long, high confidence mapped fault traces. Histogram shows the apparent strike of mapped fault segments, grouped according to distance from the Alpine fault surface trace. In the cross sections, blocks are labeled to indicate which plate they belong to and relative motions are shown, with symbol size schematically representing motion magnitude. B) This cross section shows the Alpine and Hope-Kelly faults where they are independent of each other. At this point, the Hope and Kelly faults have discrete surface traces, but intersect within the shallow sub-surface. At this distance from the Alpine fault, the Hope-Kelly system occupies the entire seismogenic depth. C) Cross section showing where the Hope-Kelly faults intersect the Alpine fault. The block between the two faults do not extend through the seismogenic crust, but ‘floats’ between the dipping faults. D) Cross section roughly perpendicular to the Hope-Kelly faults where the horsetail splay starts. This section shows how the westernmost Hope fault is a dominantly extensional fault that is antithetic to the Kelly fault splays.

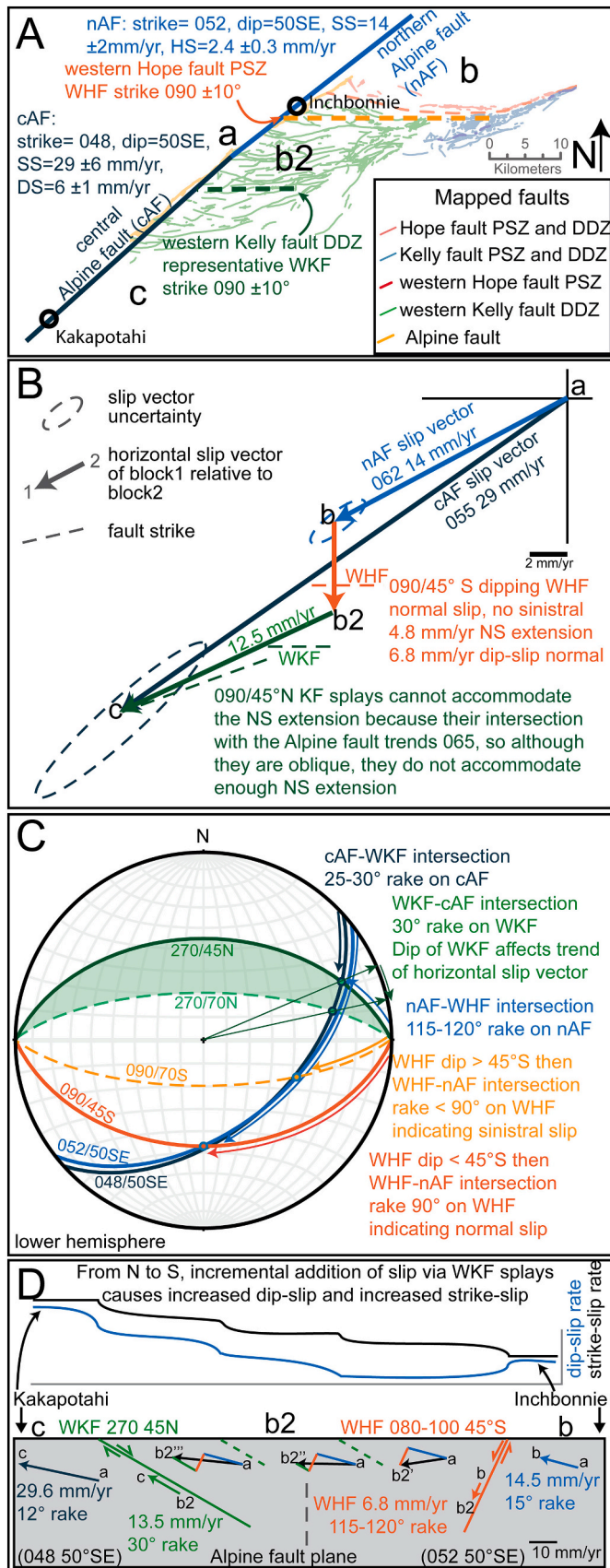
W than the strike of the fault (Fig. 13E and Fig. 15B).

We then plot the horizontal slip vectors (direction and rate relative to stationary block a) in horizontal vector space (Fig. 15B) and the distance between b and c in vector space (Fig. 15B) is the net horizontal slip deficit on the Alpine fault, ~ 15 mm/yr at 042° . This is the slip transferred off the Alpine fault onto the Hope-Kelly fault system, and it could theoretically be accommodated by a variety of fault orientations. The strike of the Western Hope fault and the Western Kelly fault are constrained by the mapping to $090 \pm 10^\circ$ within ~ 10 km of the Alpine fault where they are presumably directly intersecting the Alpine fault within seismogenic (brittle) depths. The surface dip of the Western Kelly fault splays can be imprecisely inferred to be around $45\text{--}70^\circ$ N from the interaction of the traces with topography, but there are instances of apparent southern dip direction. There is no outcrop-scale evidence for the dip of the western Hope fault.

We assume relative neutral fault intersections and then use the orientations of the central Alpine fault ($048/50$ SE) and Western Kelly faults ($270/45$ to 70 N) to determine the range of fault intersection orientations and thus the trend of the slip vector on the Western Kelly fault that would be needed to maintain rigid-block kinematics (Fig. 15C). For the vector balancing, we have chosen to use the average Western Kelly DDZ orientation, strike 090 , dip 45° N, which produces an intersection line trend $\sim 065^\circ$. Steeper dipping Western Kelly splays would result in a more E-W horizontal slip vector (Fig. 15C). The Western Kelly fault cannot accommodate the entire slip deficit of the Alpine fault because the horizontal slip vector fails to intersect the NAF vector, so it does not close the velocity circuit (Fig. 15B). Thus, some N-S extension is

necessary to balance the slip vectors and close the circuit. The remaining slip deficit may be accommodated by the western lower Taramakau Hope fault.

We know the strike of the westernmost Hope fault (WHF) is $090 \pm 10^\circ$, based on the trend of the valley and assuming the fault is within the valley, based on previous mapping of bedrock displacements across the Taramakau River (Fig. 2A; Nathan et al., 2002). The N-S extension between blocks b and b2 that is needed to complete the circuit could be accommodated by a north or south dipping normal fault striking $090 \pm 10^\circ$. Under the assumption of rigid blocks, if the WHF dips north, it would have similar kinematics to the WKF splays and similarly could not accommodate the remaining N-S extension, so to complete the horizontal slip circuit, we infer that the fault dips south and has normal or oblique slip (Fig. 15C). The intersection line between the Alpine fault (Inchbonnie $052/50$ SE) and the 090 striking, south-dipping Western Hope fault trends southward, but the range of possible Western Hope fault dip values produces a large range of intersection orientations. However, if we assume that the Western Hope fault slip vector is parallel to the intersection line and the fault has normal or dextral-normal kinematics (rake on Hope fault of 90° or more from the east), then the Western Hope fault would have to dip $\sim 45^\circ$ or less (Fig. 15C). Steeper dips would change the intersection line with the Alpine fault and imply a sinistral component of slip (Fig. 15C). Two large scale observations support the inference of normal or normal-dextral slip. First, the excess elevation of the Alexander Range to the north compared to the Bald range to the south is consistent with south-side-down faulting. Second, dip-slip displacement of the east-dipping metamorphic fabric by a south-



(caption on next column)

Fig. 15. Slip vector balancing. cAF – central Alpine fault slip vector from Kakapotahi, nAF – northern Alpine fault slip vector from Inchbonnie, WHF – Western Hope fault in the lower Taramakau River valley, WKF – generalized representation of the Hope-Kelly fault splays south of the Taramakau River. A) Map view of mapped faults and corresponding schematic faults used in this analysis. Known values are shown for each fault. SS - strike-slip rate, HS - horizontal shortening rate, DS - dip-slip rate. B) Horizontal vector diagram of the slip vectors. The vector shows the velocity (direction and rate) of the block at the arrow end, relative to the block at the start of the arrow. Vectors are colour coded with the map and the velocity and direction is noted on the diagram. The dashed lines show the direction of fault strike. C) Stereonet diagram of the average fault values used to calculate intersection orientation. Shaded areas and dashed planes show a range of fault dips that are geologically reasonable. The rake for intersections of the faults is noted with a skinny arrow and determines the kinematics of the fault. D) Schematic diagram of the Alpine fault plane with the intersections of the Western Hope fault and Western Kelly fault splays projected onto the fault plane. The slip vectors are to scale and derived from the horizontal vector diagram or known values (Inchbonnie and Kakapotahi). The vectors are calculated from the horizontal vectors, projected down onto the Alpine fault plane. They show how the net slip vector on the Alpine fault may adjust along strike as more splays of the Western Kelly fault DDZ add slip (from north to south). The top graph shows, schematically, how the strike-slip and dip-slip rate of the Alpine fault may change along strike through the intersection zone.

dipping fault will produce an apparent right separation, consistent with the geological observations of ‘dextrally’ offset metamorphic fabrics across the Taramakau River valley (Fig. 2A). Any significant sinistral displacement would mute or negate this apparent dextral sense, whereas pure normal dip-slip or normal-dextral slip rationalizes this otherwise enigmatic feature. This constrains the dip of the westernmost Hope fault to <45°S (Fig. 15C) and relative neutral intersection creates an extensional horizontal slip vector that trends $180 \pm 10^\circ$ (Fig. 15B).

We apply the Western Hope fault slip vector, assuming 45°S dip, to the horizontal slip diagram extending southward from b to b2 (Fig. 15B), and the intersection of this vector with the Western Kelly fault slip vector determines the length of both and completes the balanced slip diagram. This constrains the horizontal slip rate of the Western Kelly faults (the sum of all the splays) to ~ 12.5 mm/yr and the Western Hope fault to ~ 4.8 mm/yr. These calculations also constrain the likely dips for the Western Kelly fault splays ($\sim 45^\circ$ N, steeper dips require more slip on the WHF to complete the circuit) and the Western Hope fault ($\sim 45^\circ$ S, to accommodate N-S extension with no sinistral slip), which we use to complete the 3D fault model.

Since the intersection zone spans ~ 35 km along the Alpine fault and involves slip transfer via multiple abutting Western Kelly fault splays, the local net slip vector of the Alpine fault may change along strike across the intersection zone. Fig. 15D shows schematically the Alpine fault plane from Inchbonnie to Kakapotahi with Alpine fault local slip vectors and the orientations of the WHF and WKF intersections. This schematic shows how the slip vector of the Alpine fault changes along the intersection zone. Starting from the north, at Inchbonnie, the Alpine fault slip vector is dextral-reverse. The intersection with the Western Hope fault adds a normal oblique slip component to the dextral-reverse slip vector, nulling the reverse displacement and resulting in an Alpine fault net slip vector that is nearly horizontal. Continuing south, subsequent addition of slip from the WKF splays adds to both the dextral and reverse components of the Alpine fault slip, eventually adding to match the Kakapotahi slip vector. There may be a small number of south dipping faults with Western Hope fault-like kinematics admixed within the Western Kelly fault zone. These are not represented in the model but if present, they may take up slip that would otherwise be accommodated by the Western Hope fault, reducing its nulling effect on Alpine fault reverse displacement at the Taramakau River.

6. Analog model

6.1. Analog model methods

We use a simple analog modeling experiment as proof of concept for the 3D model and to assist in understanding the kinematics and conditions necessary to replicate the main characteristics of the fault system. The model replicates the Alpine fault and the overall Hope fault system and allows the intersectional structures to develop freely within the model medium. The Alpine fault is simulated by creating a backstop with a 45–60° dipping surface covered with waxed paper (Fig. 16A). The backstop represents the Australian plate rocks in the footwall of the Alpine fault, while the fault surface is simulated by the slick nature of the wax paper. We decided not to create the Alpine fault using an initial subduction-like deformation event, because we are more interested in the intersectional structure forming within the hanging wall than the Alpine fault itself. The central Hope fault (HFm) is simulated using a thin, stiff piece of cardboard beneath the flour that is cut so we can slide the cardboard underlying the “south” half the model, creating the strike-slip discontinuity that forms the HFm (Fig. 16A). The south cardboard base also slides beneath the AFm backstop, creating oblique

compression along the backstop ramp. The angle between HFm and AFm is 20–25°, so this configuration produces a strike-slip fault that intersects the sloped backstop creating an oblique thrust fault. The total model dimensions are approximately 15 cm wide by 20 cm long and 2–5 cm deep. The material used for the model is baking flour, which has density 1200 kg/m³ and cohesion 330 Pa, and internal friction angle 0.29° (Krantz, 1991; Acocella, 2005; Tibaldi et al., 2006; Buitert, 2012; Reber et al., 2020). We chose this material because the high cohesion allows faults to be observed without particle tracking, which would have been necessary to map deformation in cohesionless granular materials. The small grain size is necessary to scale with the small model size, although we did not apply any precise scaling to this model.

We did multiple repeats of the model. The model is powered by hand, so displacement rates were not quantified. In some repeats the flour was lightly compacted and placed by hand, and in some repeats the flour was dropped into the model through a sifter to avoid forming any unintended pre-existing structures by variable compaction of the flour. We did not purposely simulate any pre-existing structures or variations in material strengths that may have simulated bedrock fabric or composition. We did not include any simulations of erosion or deposition during deformation. We tested the ideal angle between AFm and HFm between

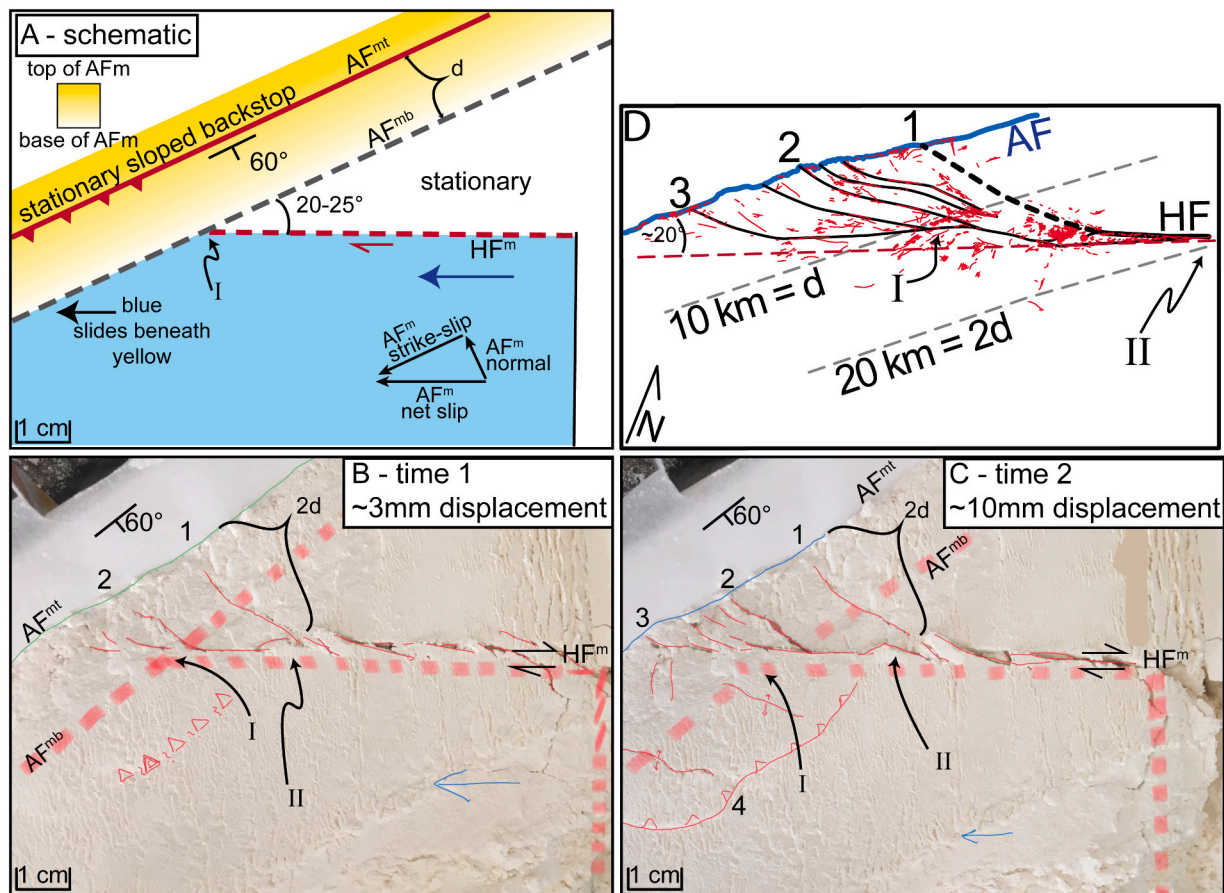


Fig. 16. A) Analog model set-up in plan view. HFm represents the model Hope fault, strike slip motion is simulated by sliding the thin cardboard (blue) in the direction of the arrow. AFm represents the model Alpine fault and is created by a 60° dipping wax paper surface (yellow) oriented 20–25° counter-clockwise from HFm. Because of the dip, the surface trace (AFmt) of AFm is horizontally offset from the basal velocity discontinuity (AFmb). The two faults (HFm and AFmb) meet at the base at point I. The horizontal distance between AFmt and AFmb is d . B) Faults formed in the flour model material after small (~3 mm) displacement along HFm. Surface fault traces are marked in thin red lines, locations of the basal faults are shown with transparent thick dashed red lines. Riedel shears have formed on HFm, but near the intersection with AFmb (point I), these shears lengthen toward AFmt and rotate slightly more orthogonal to AFm (1 and 2). The HFm surface trace does not reach the AFm surface trace. C) With more displacement on HFm (~10 mm), the fault becomes more continuous, and extends further toward AFmt. Faults 1 and 2 have lengthened and have more extension on them. New AFm orthogonal splay faults have formed between HFm and AFmt (i.e. 3) south of the initial splay faults. Also, an AFm antithetic thrust fault has formed parallel to AFm and some contractional folds have formed subparallel to the HFm splays (1,2,3). D) Map view of the study area, labeled with locations corresponding to features in the analog model. Mapped faults are shown in red, and modeled fault traces are black. (For interpretation of the references to colour in this figure legend, the reader is referred to the web version of this article.)

20 and 25°, but also angles between 10 and 45°. We modeled small components of both compression and extension on HFm, and that combined with the angle between HFm and AFm produced varying obliquity on AFm. The specific model repeat we present in the results has ~25° angle between HFm and AFm with no transtension or transpression across HFm (Fig. 16B and C).

6.2. Analog model results

The analog model replicates the central Hope fault (HFm) and the Alpine fault (AFm) and produces structures in the AFm-HFm junction area with orientations and transtensional kinematics that match those observed and inferred for the Western Kelly faults and the Western Hope fault (Fig. 16B, C and D). The central Hope fault in the analog model (HFm) first forms en-echelon Riedel shears, then P shears that coalesce to eventually form a through-going principal slip zone in the area away from the AFm backstop (Fig. 16B).

We define a distance d , the width of the Alpine fault ramp, in both the real fault world and the analog model. At distance $2d$ (Fig. 16B, point II) from the Alpine fault model trace (AFmt) (i.e. twice the fault width to the base of the ramp), the Riedel shears of HFm diverge from their ideal strike and extend further toward the AFmt, eventually meeting it nearly orthogonally (Fig. 16B and C - markers 1 and 2). As HFm displacement increases, new Riedel-like shears form along the projection of HFm, but above the AFm fault ramp (Fig. 16C - marker 3). These HFm shears accommodate dextral-normal oblique displacement and the new shears are progressively shorter in length as the projection of HFm converges on AFmt (Fig. 16C - marker 3). At distance $2d$ from the AFmt within the moving (right side) block, an AFm antithetic thrust fault forms (Fig. 16C - marker 4), accommodating some of the shortening component of oblique convergence.

Through multiple runs of the model, we found that the angle between the Alpine fault and the Hope fault was critical to formation of the horsetail structure. When the angle between the Hope and Alpine faults was more than 30°, the horsetail splay did not form but a single HFm trace met discretely with the AFmt. Also significant was the packing of the flour, if it was sifted into the model, the horsetail splaying was more diffuse and more fault splays formed, but if the flour had been compacted at all, only 1–3 larger displacement splay faults formed, still with the general structure of the horsetail splay. This suggests that the shear strength (aka cohesion) of the material in the hanging wall wedge is also a significant factor in forming the horsetail. When the model material is more granular, the model faults better represent the real fault system, this suggests that the continuous tectonic strain and transient strains associated with earthquakes provide mechanisms for sustaining the highly fractured rock mass with high fault density that we observe in nature. Finally, no pre-existing structures were needed to form the horsetail splay, it is caused by the overall geometry and kinematics of the two interacting faults and their spatial and angular relation to each other.

7. Discussion

7.1. Characteristics of the Hope-Kelly fault system

The new mapping and modeling presented here reveals a branching fault system with increasing structural and kinematic complexity toward the Alpine fault in the region between the previously mapped Taramakau section of the Hope fault and the Kelly fault, (Fig. 2B and 14). The characteristics of this fault system are best described with respect to distance from the Alpine fault surface trace, measured perpendicular to the Alpine fault strike. At Harper Pass (20 km from Alpine fault) and in the upper Taramakau valley, the principal slip zones of the Hope and Kelly faults are subparallel, strike ~070° and have dextral slip. The extensive secondary faulting expressed geomorphically and the fault rocks in the riverbed indicates that the two faults interact structurally in

the upper crust beneath the upper Taramakau River valley, and slip may be transferred between them on a variety of spatial and temporal scales (section 4.1). The NE-striking faults between the Hope and Kelly faults, described in section 4.4. (Sackung Hill, Fig. 9, located 15 km from Alpine fault), likely transfer dextral slip from the Hope fault to the Kelly fault. The Hope and Kelly faults gradually diverge, and the Hope fault has no localized surface expression west of Michaels Creek (Figs. 7, 15 km from Alpine fault), though there are indirect geomorphic features that may indicate an active, north side up fault within the lower Taramakau River valley (section 4.2.). West of the Kelly Range (Figs. 10, 10 km from Alpine fault), the faults splay and the strikes generally transition to ~090 (Fig. 14A), and apparent displacements are dextral-normal. These faults are often discontinuous due to limitations of mapping on the pDSM, but they do show significant (10+ m) displacement and sections of prominent geomorphic expression indicative of tens of meters of total slip on each of these faults since the landscape was refreshed in the last glaciation (Ivy-Ochs et al., 1999; Barrows et al., 2013; Eaves et al., 2017). That these fault traces have any geomorphic expression preserved in this extremely active landscape indicates that they must have a high slip rate and frequent ruptures (Cox et al., 2012). We have modeled 4 distinct splays of the Western Kelly fault DDZ within the westernmost 10 km, however, they are not the only faults but rather idealized planes representing the longest and most continuous mapped faults with strongest surface expression. Many more discontinuous faults are also mapped in this area and it is likely more would be revealed with more extensive lidar coverage. We have mapped a splay of the Western Kelly fault DDZ, previously mapped as the Hura fault (Nathan et al., 2002), intersecting the Alpine fault with co-mingling surface rupture traces (Figs. 11 and 12), indicating that the Western Kelly faults do indeed physically abut the Alpine fault.

7.2. Lower Taramakau Hope Fault

The Western Hope fault forms the north side of the intersection zone “triangle” and extends up to the surface from where the N dipping Kelly and E dipping Alpine fault meet within seismogenic depths (Fig. 14). South of the Hope fault, the crustal block is within the hanging wall of the Alpine fault and subject to the oblique (dextral-normal) faulting of the Western Kelly fault DDZ horsetail splay. We consider the lower Taramakau, EW-striking section of the Hope fault to be decoupled from the strike-slip component of the fault system, as neither the footwall nor hanging wall are fully coupled to the Pacific Plate south of the Kelly fault. The Hope fault is likely nearly pure dip-slip normal if it dips <45°. Despite the lack of discrete surface expression, it is possible this fault remains active and contributes to the seismic moment of major earthquakes in this region.

7.3. Cause and significance of gravitational secondary faulting

The ability of a simple analogue model to represent the observed first-order structures of the Hope-Kelly-Alpine fault interaction zone shows that the geometry and resultant kinematics (i.e. formation of the horsetail splay) can be attributed to the interaction between the Hope, Kelly and Alpine faults, and is strongly modulated by the geometry of these principal faults relative to each other (Fig. 16). However, secondary gravitational faults (Section 4.4., Fig. 9) are not expressed in the analog model and are not well explained by the tectonic fault interactions. So, although the first order fault geometry and kinematics are of purely tectonic origin, second order faulting is due to a combination of first order process and seismic shaking, topographic amplification, and geomorphic history (e.g., gravitational collapse features; Beck, 1968; Pere, 2009). Gravitational faults have been modeled to be able to occur in mountains with certain shapes driven by gravitational forces alone (Li et al., 2010; Kinakin and Stead, 2005; Savage and Varnes, 1987), but others have found the gravitational faults to be concentrated in areas of high tectonic activity and have even related displacement on

them to individual proximal paleo-earthquakes (Komura et al., 2017; Gold et al., 2019). The mountain ranges in the study region are densely dissected by faults and are situated in a region of high seismic shaking hazard, as indicated from 10% probability of 0.8 to 0.9 g peak ground accelerations being exceeded in 50 years (Stirling et al., 2012). Together with spatiotemporal variations in surface mass distributions associated with glacial-interglacial cycling and their effects on topography, and the high rainfall regional climate, the tectonic and climatic processes conspire to generate a highly dynamic landscape. Topographic adjustments in response to extrinsic forcing and stress variations are superimposed on to, and associated with, seismic slip on faults and associated strong shaking. Spatial variances in the geometry and kinematics of gravitational faults and landslides are likely also to be influenced by processes including glacial de-buttressing and oversteepening of mountain flanks, variations in prevailing azimuths and intensities of seismic ground motions, and other factors that influence landscape stability. Sackung hill and the Kelly Range (Figs. 7 and 9) are characterized by low relief summits that are heavily fractured by sackung and tectonic fault meshes that collectively accommodate distributed summit collapse, and steep flanks dominated by landsliding but with possible topographic bulging. We propose that the Sackung Hill provides an example of how an incipient fault system begins to form through the summit of a mountain range, with the expectation that continued deformation localization and gravitational faulting may focus denudation here and eventuate in the topographic destruction of the existing

range.

7.4. Southern Alps orogen affects Hope-Kelly fault structure

7.4.1. Eastern edge of the orogen

In the central Southern Alps, the highest contemporary uplift rates occur between ~12–18 km from the Alpine fault and gradually reduce to the east, remaining above 2 mm/yr up to ~30 km from the Alpine fault (Beavan et al., 2004). The surface traces of the Main Divide Fault Zone (MDFZ), the most proximal reverse fault zone antithetic to the Alpine fault, are located ~15–20 km from the Alpine fault surface trace (Fig. 17A) (Findlay, 1980; Cox and Findlay, 1995; Becker and Craw, 2000; Nathan et al., 2002; Cox and Barrell, 2007; Upton et al., 2004; Cox et al., 2012). The MDFZ develops as a result of bending of the Pacific Plate crust as it begins to traverse the Alpine Fault Ramp (Cox and Findlay, 1995). Both the eastern edge of the Southern Alps high uplift zone and the MDFZ are approximately the same distance from the Alpine fault as the splaying of the Kelly Fault from the Hope Fault at Harper Pass, suggesting that the structure of the Hope fault system is influenced by the Alpine fault transforming horizontal plate motion into orogenic uplift.

7.4.2. Direct interaction with the Alpine Fault

Based on analysis of geodetic strain rates, Haines and Wallace (2020) propose that the surface projection of the down-dip locked extent of the

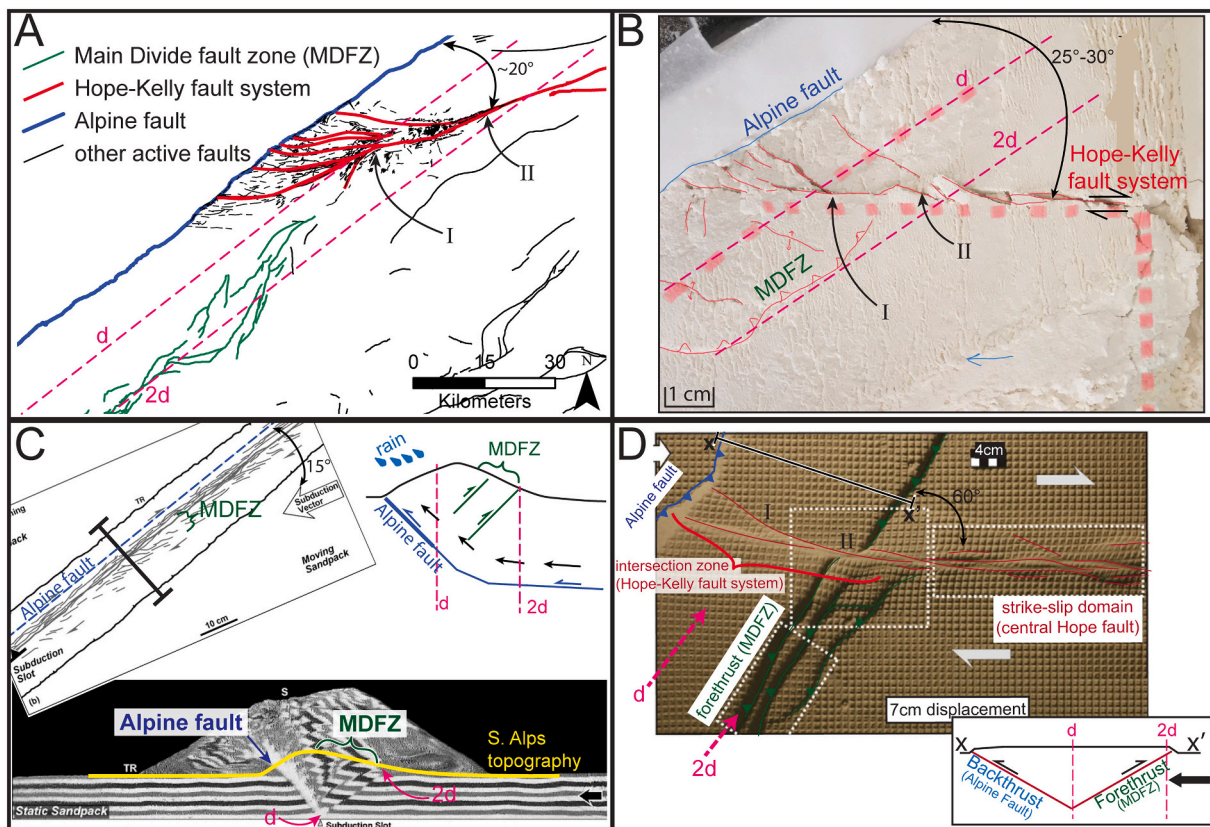


Fig. 17. Comparison between the Hope-Kelly fault system and analog modeling. A) Major faults of the Southern Alps, colour coded for reference. Distance d is ~10 km from the Alpine fault surface trace and represents the eastern extent of the seismogenic Alpine fault and is coincident with formation of the Hope-Kelly horsetail splay. Distance $2d$ is ~20 km from the Alpine fault and is coincident with the position of the Main Divide Fault Zone and the eastern extent of maximum contemporary uplift from Beavan et al. (2004). B) The analog model from this study, oriented to coincide with map A. Distances d and $2d$ are shown and coincide with the horsetail splay and the initial formation of the Kelly fault, respectively. The Alpine fault antithetic thrust is analogous to the MDFZ. C) Map view and cross section of the highly oblique (15°) convergence analog model from McClay et al., 2004. D) Model and annotation of the 60° thrust-wrench interference analog model from Rosas et al. (2012), oriented so the strike-slip fault is parallel to the real Hope fault in A. In this model, the backthrust is analogous to the Alpine fault, as shown in the X-X' schematic cross section. Distance d in this model corresponds to the basal velocity discontinuity producing the thrust wedge and $2d$ is the edge of the pro-wedge (forethrust), and the MDFZ would occur near $2d$. The Hope-Kelly fault system corresponds to the extensions of the strike-slip fault through the thrust wedge. Positions I and II are indicated and correspond to those in A and B.

Alpine Fault is ~10 km east of the Alpine fault surface trace (Fig. 15D). Using a simple geometric calculation based on the depth of the seismogenic zone (8 to 12 km deep for the Alpine fault, ~15 km deep in MFS) (Leitner et al., 2001; Michailos et al., 2019) and the generally accepted range of dip for the Alpine fault (45–60 degrees; Langridge et al., 2010; Cox et al., 2012; Barth et al., 2013), the easternmost horizontal extent of the seismogenic Alpine fault, where it projects vertically to the surface, is within 15 km of the surface trace, and more likely around 10 km (Fig. 15D). West of this point, the surface traces of Hope and Kelly faults start to significantly diverge and form multiple splays and modal fault strike transitions from ~070° to ~090° as the faults curve and become more perpendicular to the Alpine fault (Fig. 14). This spatial correlation between kinematic and structural zones of the Hope-Kelly fault system with the bivergent plate boundary zone and direct interaction with the seismogenic Alpine fault, support the interpretation that both kinematic interactions and direct intersections between the Hope-Kelly and Alpine faults are responsible for the observed horsetail splay at the surface, consistent with the simple analogue model results.

7.4.3. Effect of the orogen on stress directions

The stress field in a region is predominantly governed by far field stresses, topographic stresses and crustal rheology. The regional maximum horizontal compressive stress, inferred from earthquake focal mechanisms (Townend et al., 2012; Michailos et al., 2020), and geologically determined (Nicol and Wise, 1992; Pettinga and Wise, 1994) is sub-horizontal and oriented ~115°. Fault kinematics can act to perturb stresses locally, as commonly seen in situations like pop up and graben structures along strike-slip faults (Wood et al., 1994). The change from strike-slip on the central Hope Fault to reverse oblique slip on the Alpine Fault is a larger scale example of this perturbation as the reverse slip and orogenesis associated with the Alpine fault transform horizontal rock velocities into vertical. The strike-slip on the Hope Fault implies σ_2 is vertical whereas oblique slip on the Alpine Fault requires σ_3 to be steeply inclined and may be similar in magnitude to σ_2 . This is borne out by the stresses inferred from earthquake focal mechanisms, as the intermediate and minimum principal stresses (σ_2 and σ_3 , respectively) are nearly equal in magnitude and rotate between vertical and horizontal over short distances as the plate boundary fault system evolves from primarily strike-slip (σ_2 vertical) in the east to dextral-reverse oblique along the Alpine fault (σ_3 sub-vertical, inclined NW and σ_2 inclined southeastward, along the Alpine Fault plane). Although stress directions inferred from small to medium magnitude earthquakes may not be representative of the regional stress orientations, the consistency between the kinematics of the principal faults and stress directions inferred from focal mechanisms gives us confidence in our interpretation of the fault interactions. Within the Hope-Kelly fault system the majority of faults are contained within the intersectional process zone of the horsetail splay and may not be subject to forcing primarily by regional stresses. Oblique normal faulting on the Western Kelly fault DDZ results from removal of support by southward translation of the central Alpine Fault hanging wall that reduces horizontal stresses and leaves σ_1 sub-vertical. Thus, within the intersection zone, the faults are controlled by stresses resulting from the interaction of the principal faults. Each of these local stress changes are driven by the kinematics of the component faults within the far-field stress regime.

7.4.4. Alpine Fault slip rate change and rock particle velocities

The east to west transition of the Kelly fault splays, from dextral to dextral-normal oblique kinematics, is interpreted to result from the underlying east-dipping Alpine fault converting horizontal crustal velocities associated with plate motion into vertical uplift. Rock particles moving toward the Alpine Fault transition from horizontal to oblique upward trajectories as they ascend the fault ramp (Koons, 1990; Herman et al., 2007). By dissecting the central and northern Alpine fault hanging walls, the Hope-Kelly fault system defines a zone that can accommodate the variations in horizontal and vertical rock velocities resulting from

the differences between central and northern Alpine fault slip rates. Because all blocks within the Hope-Kelly-Alpine Fault wedge are being advected up the Alpine Fault, albeit at different rates, rock uplift is expected adjacent to and throughout the crustal wedge, but variations in uplift rate are accommodated by obliquely slipping faults with a normal component. The exact net slip vector for the Alpine fault at any point within the intersection zone depends on how the slip is partitioned among the north-dipping and south-dipping splays of the Hope-Kelly fault system (Fig. 15D). If all the necessary NS extension is accommodated on the south-dipping westernmost Hope fault alone, the Alpine fault immediately south of that intersection could theoretically be pure strike-slip, with reverse slip accruing southward by normal displacement on the north-dipping Western Kelly fault splays. Further clarification of the Alpine fault net slip at any point would require more detailed site specific investigations within the intersection zone, which should motivate further lidar surveys of that area.

7.5. Comparison with analog models

The discussion above highlights the importance of two key locations – the first being the splaying of the Hope and Kelly at Harper Pass, ~20 km from the Alpine fault, and the second being the development of multiple Western Kelly fault splays and Western Hope fault striking sub-perpendicular to the Alpine Fault within 10–15 km of the Alpine Fault surface trace. These two critical points are replicated in the analog model. At position II (Fig. 16), ~2D distance from the modeled trace of the Alpine fault (AFmt), the modeled central Hope fault (HFm) splits into two faults, one striking roughly parallel to the underlying velocity discontinuity that forms HFm, and one roughly orthogonal to the AFm. We consider this to be analogous to the splaying of the Hope and Kelly faults at Harper Pass, 18 km from the Alpine fault, measured perpendicular to the Alpine fault strike. At the surface projection of the basal intersection of the model Alpine and Hope Faults (Fig. 16A, point I at distance d from AFm), the model Hope Fault develops multiple splays sub-perpendicular to the model Alpine Fault, and the number of splays increases with displacement on the Hope Fault. We consider this to be analogous to the EW splaying of the Kelly Fault.

Similar geometries are implicit or explicitly reported in previous analog modeling studies ((Fedorik et al., 2019; McClay et al., 2004; Rosas et al., 2012, 2015). Analog modeling of highly oblique convergence (Fig. 17C) by McClay et al. (2004) demonstrates that at convergence angles less than 30°, the backthrust (i.e. the retro-thrust or the wedge-bounding thrust that dips toward convergence) is the dominant structure, remaining stationary and slipping throughout orogenesis, while the forethrusts accumulate relatively small total displacements and are quickly advected through the wedge and replaced by new forethrusts. If this model is considered in terms of the Southern Alps, the overriding of the wedge onto the footwall and partitioning of the strike-slip and thrust components within the retrowedge would not occur as the orographic erosion stops the thrust wedge from overriding the footwall. This in turn pins the surface trace at the base of the range and combined with high heat flow on the Alpine fault concentrates the oblique deformation onto a single fault (Batt and Braun, 1997; Ellis et al., 2001; Koons et al., 2003). The significance of the backthrust dominance becomes apparent when we look at the models of Rosas et al., 2012, 2015, Fig. 17D, where they look at thrust-strike-slip interference structures. In their model with 60° between the strike-slip fault (created by two adjacent base plates that can move laterally relative to each other) and the thrust fault (created by sliding both strike-slip base plates beneath a stationary plate, simulating subduction), the strike-slip fault interacts primarily with the forethrust splays (Fig. 17D, position II) becoming forethrust parallel and merging with new forethrusts. There are no similar structures in the Southern Alps, likely owing to the ~20° convergence angle, which McClay's model demonstrates results in less forethrust development than a 60° convergence angle (Fig. 17C). In Rosas et al. model, the strike-slip fault propagates through the doubly

vergent thrust wedge, and between d and 2d it splays and turns to become more orthogonal to the backthrust, similar to the curved faults of the Hope-Kelly fault system. The strike-slip splay faults within the thrust wedge have oblique slip to accommodate the differential growth of the thrust wedge. This is analogous to the Alpine fault slip rate change and resulting differential topographic growth orthogonal to the Hope-Kelly fault system that causes dextral-normal oblique slip on the horsetail splays.

7.6. Implications for the formation of MFS faults

The propagation direction during the formation of the Hope fault is a question that has yet to be solved. The MFS in general is occasionally referred to as a system of “splays” of the Alpine fault (Hatem et al., 2019; Scholz et al., 2010; Silberling et al., 1988). This implies that their genesis lies along the Alpine fault and they have propagated east from there. However, the abutting structure of the Hope-Kelly fault system against the Alpine fault suggests a westward propagation of the fault system, because the younger faults do not actually branch off the Alpine fault. The concept of “first-order splay faults” of Scholz et al. (2010) may be more applicable to the Hope fault, and by extension the other major members of the MFS. First order splay faults (Scholz et al., 2010) are suggested to form initially at a distance from the parent fault (the Alpine fault) and propagate toward the parent fault and may or may not ever physically intersect. The Clarence fault, the next branch of the MFS north of the Hope fault (see Fig. 1) has been mapped as terminating east of the Alpine fault and not intersecting the Alpine fault at the surface, so maybe the Hope fault formed before the Clarence could fully propagate west to form a direct fault intersection. First-order splay faults may form as a result of the parent fault becoming misoriented with respect to the regional stress, either as a result of fault rotation or far field changes in plate motions. The Alpine fault is thought to have evolved from a purely strike-slip dextral fault to become a dextral-reverse fault in the last ~8.5 my due to a shift in the Euler pole of the Pacific plate relative to the Australian plate (Little and Jones, 1998; Walcott, 1998; Batt et al., 2004). This is around the time when the MFS began to form, initially with the Awatere fault ~5–7 Mya (Little and Jones, 1998), the Clarence and finally the Hope fault formed 0.6–1.6 Mya (Wood et al., 1994; Langridge et al., 2013). While the Alpine fault is oriented slightly oblique to the relative plate motions, the western faults of the MFS are overall roughly parallel to the relative plate motion and thus more optimally oriented for strike-slip, a principle of the first-order splay fault paradigm. If this is indeed the formation mechanism of the MFS, it suggests that the next MFS fault will form in the central part of the South Island, east of the Southern Alps, and south of the Hope fault. As has been previously identified, the Porters Pass-Amberley fault zone (Fig. 1) meets these criteria and our findings support the assertion that these faults define an incipient MFS fault and thus mark the location of a future major plate boundary fault (Cowan et al., 1996; Little and Jones, 1998).

7.7. Comparison of the Hope-Kelly fault system with other fault intersections

Comparisons of the Hope-Kelly-Alpine intersection with other continental scale synthetic strike-slip fault intersections shows fundamental differences. The Denali-Totschunda intersection consists of a discrete junction (<1 km of Riedel fault interaction between the faults) of the two vertical fault planes with 28–30° difference in strike. The Totschunda fault has transitional complexities along the northwestern ~25 km that are limited to an 8 km wide zone and do not extend toward the Denali fault (Haeussler et al., 2004; Ratchkovski et al., 2004; Schwartz et al., 2012). At the intersections of the San Andreas fault with the Calaveras, San Gregorio, and San Jacinto faults, the faults approach with ~20° difference in strike and bend to have nearly parallel strikes within ~10 km of each other (Morton and Matti, 1993; Bruns et al., 2002; Watt

et al., 2014). There are extensional basins within the acute angle of the San Gregorio-San Andreas and San Jacinto-San Andreas intersections, however, if any of these intersections have structures involving linking, synthetic faults that strike sub-perpendicular to the main faults, they are much smaller in spatial extent than the Hope-Kelly fault system (i.e. Watt et al., 2014). The most fundamental difference between these various continental scale synthetic strike-slip fault intersections and the Hope-Kelly-Alpine intersections is that the other faults are all vertical strike-slip faults with little dip-slip. Although the plate boundaries are similarly transpressional, the slip is partitioned onto separate strike-slip and compressional structures (Spotila et al., 2007; Bemis et al., 2015). In the Hope-Kelly-Alpine intersection, the oblique reverse slip and moderate to low dip of the Alpine fault promote formation of a kinematically complex and spatially expansive intersectional zone that is apparently unnecessary to accommodate slip transfer between near-vertical strike-slip faults. These factors (slip partitioning of transpressional plate boundaries and vertical strike-slip faults) are likely the critical differences between the Hope-Kelly-Alpine intersection and that of other synthetic strike-slip fault intersections that do not have similarly complex or spatially expansive intersection zone structures.

8. Conclusions

New mapping of the Taramakau section of the Hope fault and Kelly fault (Hope-Kelly fault system) reveals the transition from a relatively simple dextral fault (Hurunui and Hope River sections of the central Hope Fault) to an increasingly dispersed and structurally complex horsetail splay network. Dominant fault strike and kinematics transition from ~070° and pure dextral in the east to ~090° and dextral-normal in the west as Western Hope and Western Kelly fault splays approach the Alpine fault. Co-mingling of individual Western Kelly fault splays with the Alpine fault at the surface demonstrates that the faults physically intersect and abut the Alpine fault in 3D. Splaying and kinematic changes of the Hope-Kelly fault system correlate spatially with the surface projection of the Alpine fault at the base of the seismogenic zone (10–15 km deep), indicating that geometric and kinematic interactions between the Alpine fault and the younger Hope-Kelly fault system at depth exert a primary influence on surface rupture geometry of the Hope-Kelly fault system.

Where the Hope-Kelly system diverges into the horsetail structure, most of the strike-slip motion of the Hope fault in the upper Taramakau River valley is transferred onto the Kelly fault and subsequently distributed throughout the horsetail splay. The Hope to Kelly slip transfer is accomplished through coeval NW and EW-striking dextral faults exemplified on Sackung Hill. Extension of the Alpine fault hanging wall via normal slip on the Western Hope fault and oblique normal-dextral slip on the horsetail splays allows the slip rate change between the central and northern Alpine fault.

While structurally complex, the Hope-Kelly horsetail structure forms as a result of simple parent fault geometry, demonstrated by simple analog modeling. The horsetail splay efficiently transfers slip to the Alpine fault via relative neutral fault intersections requiring minimal inter-fault block volume changes. Gradual rake rotation on the Kelly fault splays merges the dextral central Hope fault with the dextral-reverse oblique Alpine fault. The reverse component of slip on the Alpine fault causes rock particle velocities shift from horizontal to uplifting within the Southern Alps orogen. The normal component of slip on the horsetail splays accommodates differential orogenic uplift resulting from the Alpine fault slip rate change.

Topographic stress perturbations in steep terrain promotes formation of gravitational faults, which form complex fault networks within topographic highs. Where these gravitational faults interact with tectonic faults, they may cause fault rake changes, obscuring the true kinematics of the tectonic faults.

The Hope-Kelly/Alpine fault intersection is unique among continental strike-slip plate boundary fault intersections because the Alpine

Fault is a truly obliquely slipping fault, which allows the intersection to form with neutral fault intersections that efficiently accommodate and transfer the slip of both parent faults. If the relative plate motion currently accommodated by the Alpine Fault were partitioned onto separate strike-slip and compressional structures, the intersection structure would be expected to exhibit different geometries and kinematics to those observed in this study.

Declaration of Competing Interest

The authors declare that they have no known competing financial interests or personal relationships that could have appeared to influence the work reported in this paper.

Acknowledgements

We thank the New Zealand Earthquake Commission for funding the lidar acquisition component of this research through an Earthquake Commission Capability Fund grant to JRP and MQ. RML was funded through GNS Science research projects TSZ and ZLD 2.2.2 South Island Paleoseismology, and the Alpine fault lidar acquisition was funded by the Natural Hazards Research Platform (NHRP). JV acknowledges the support of a University of Melbourne International Research Scholarship and the Baragwanath Trust. Additional funding for this research was provided through an Australian Research Council Discovery Project Grant (#DP170103350). Permits for sampling and field work were provided by the Department of Conservation (DOC). Seequent generously provided access to the Leapfrog Geo© software. We thank the property owners Ed and Michelle Evans for access to their properties and for lodging and logistical support. We thank Andrew Wilson, Santosh Dhakal, Naomi Leclere, Mindi Curran, and Hector Flores for field assistance. We thank Eric Cowgill and an anonymous reviewer for their extensive and constructive reviews that helped us substantially improve the manuscript. We acknowledge Kāti Wairaki and Ngāi Tahu as first peoples of Nōti Taramakau and Kā Tiritiri-o-te-moana.

Appendix A. Supplementary data

Supplementary data to this article can be found online at <https://doi.org/10.1016/j.tecto.2021.228928>.

References

- Acocella, V., 2005. Modes of sector collapse of volcanic cones: insights from analogue experiments. *J. Geophys. Res. Solid Earth* 110, 1–19. <https://doi.org/10.1029/2004JB003166>.
- Adams, J., 1980. Contemporary Uplift and Erosion of the Southern Alps, New Zealand. *GSA Bull.* 91, 1–114. <https://doi.org/10.1130/GSAB-P2-91-1>.
- Allen, S.K., Cox, I.S.C., Owens, I.F., 2011. Rock Avalanches and Other Landslides in the Central Southern Alps of New Zealand: A Regional Study Considering Possible Climate Change Impacts, pp. 33–48. <https://doi.org/10.1007/s10346-010-0222-z>.
- Altamimi, Z., Rebischung, P., Métivier, L., Collilieux, X., 2016. ITRF2014: a new release of the International Terrestrial Reference Frame modeling nonlinear station motions. *J. Geophys. Res. Solid Earth* 121, 6109–6131. <https://doi.org/10.1002/2016JB013098>.
- Ando, R., Tada, T., Yamashita, T., 2004. Dynamic evolution of a fault system through interactions between fault segments. *J. Geophys. Res. Solid Earth* 109, 1–15. <https://doi.org/10.1029/2003JB002665>.
- Arnadottir, Thora, Beavan, John, Pearson, Chris, 1995. Deformation associated with the 18 June 1994 Arthur's Pass earthquake. *New Zealand Journal of Geology and Geophysics* 38 (4), 553–558. <https://doi.org/10.1080/00288306.1995.9514682>.
- Barnes, P.M., Audru, J.-C., 1999. Recognition of active strike-slip faulting from high-resolution marine seismic reflection profiles: Eastern Marlborough fault system, New Zealand. *Geol. Soc. Am. Bull.* 111, 538–559. [https://doi.org/10.1130/0016-7606\(1999\)111<0538:ROASSF>2.3.CO;2](https://doi.org/10.1130/0016-7606(1999)111<0538:ROASSF>2.3.CO;2).
- Barrell, D.J.A., Andersen, B., Denton, G., 2011. Glacial geomorphology of the central South Island, New Zealand. *GNS Sci. Monogr.* 27. <http://shop.gns.cri.nz/mon27/>.
- Barrows, T.T., Almond, P., Rose, R., Keith Fifield, L., Mills, S.C., Tims, S.G., 2013. Late Pleistocene glacial stratigraphy of the Kumara-Moana region, West Coast of South Island, New Zealand. *Quat. Sci. Rev.* 74, 139–159. <https://doi.org/10.1016/j.quascirev.2013.04.010>.
- Barth, N.C., Toy, V.G., Langridge, R.M., Norris, R.J., 2012. Scale dependence of oblique plate-boundary partitioning: new insights from LIDAR, central Alpine fault, New Zealand. *Lithosphere* 4, 435–448. <https://doi.org/10.1130/L2011.1>.
- Barth, N.C., Boulton, C., Carpenter, B.M., Batt, G.E., Toy, V.G., 2013. Slip localization on the southern Alpine Fault, New Zealand. *Tectonics* 32, 620–640. <https://doi.org/10.1002/tect.20041>.
- Batt, G.E., Braun, J., 1997. On the thermomechanical evolution of compressional orogens. *Geophys. J. Int.* 128, 364–382. <https://doi.org/10.1111/j.1365-246X.1997.tb01561.x>.
- Batt, G.E., Baldwin, S.L., Cottam, M.A., Fitzgerald, P.G., Brandon, M.T., Spell, T.L., 2004. Cenozoic plate boundary evolution in the South Island of New Zealand: new thermochronological constraints. *Tectonics* 23. <https://doi.org/10.1029/2003TC001527>.
- Beavan, J., Matheson, D., Denys, P., 2004. A vertical deformation profile across the Southern Alps, New Zealand, from 3.5 years of continuous GPS data. In: *Proceedings of the Cahiers du Centre Européen de Géodynamique et de Séismologie workshop: The State of GPS Vertical Positioning Precision: Separation of Earth Processes by Space Geodesy*, Luxembourg, v. 23, pp. 111–123. <http://www.colorado.edu/geolsci/faculty/molnarpdf/2004Luxembourg.BeavanNZ-VertGPS.pdf>.
- Beck, A.C., 1968. Gravity faulting as a mechanism of topographic adjustment. *N. Z. J. Geol. Geophys.* 11, 191–199. <https://doi.org/10.1080/00288306.1968.10423684>.
- Becker, J.A., Craw, D., 2000. Structure and neotectonics on the main divide, upper Wilberforce valley, mid Canterbury, New Zealand. *New Zeal. J. Geol. Geophys.* 43, 217–228. <https://doi.org/10.1080/00288306.2000.9514882>.
- Bemis, S.P., Weldon, R.J., Carver, G.A., 2015. Slip partitioning along a continuously curved fault: quaternary geologic controls on Denali fault system slip partitioning, growth of the Alaska Range, and the tectonics of south-central Alaska. *Lithosphere* 7, 235–246. <https://doi.org/10.1130/L352.1>.
- Berryman, K., Villamor, P., 2004. Surface rupture of the Poulter Fault in the 1929 March 9 Arthur's Pass earthquake, and redefinition of the Kakapo Fault, New Zealand. *New Zeal. J. Geol. Geophys.* 47, 341–351. <https://doi.org/10.1080/00288306.2004.9515060>.
- Berryman, K.R., Beanland, S., Cooper, A.F., Cutten, H., Norris, R., Wood, P.R., 1992. The Alpine Fault, New Zealand: Variation in Quaternary structural style and geomorphic expression. *Annales Tectonicae* VI, 126–163.
- Berryman, K., Rattenbury, M., Beavan, J., Isaac, M., Villamor, P., Van Dissen, R.J., 2003. Active faulting and strain accumulation at the junction of the Alpine and Hope faults, New Zealand. In: *Geological Society of New Zealand Annual Conference*, pp. 37–38.
- Bruns, T.R., Cooper, A.K., Carlson, P.R., McCulloch, D.S., Parsons, T., 2002. Structure of the Submerged San Andreas and San Gregorio Fault zones in the Gulf of the Farallones off San Francisco, California, from High-Resolution Seismic Reflection Data. In: Parsons, T. (Ed.), *Crustal Structure of the Coastal and Marine San Francisco Bay Region*, California, pp. 77–117. US Geological Survey Professional Paper, 1658.
- Buiter, S.J.H., 2012. A review of brittle compressional wedge models. *Tectonophysics* 530–531, 1–17. <https://doi.org/10.1016/j.tecto.2011.12.018>.
- Burbank, D.W., Anderson, R.S., 2011. *Tectonic*. Chichester, UK, John Wiley & Sons, Ltd, Geomorphology. <https://doi.org/10.1002/9781444345063>.
- Carpentier, S.F.A., Green, A.G., Langridge, R.M., Hurter, F., Kaiser, A., Horstmeyer, H., Finnemore, M., 2013. Seismic imaging of the Alpine Fault near Inchoibonnie, New Zealand. *J. Geophys. Res. Solid Earth* 118, 416–431. <https://doi.org/10.1029/2012JB009344>.
- Chaussard, E., Bürgmann, R., Fattahi, H., Nadeau, R.M., Taira, T., Johnson, C.W., Johanson, I., 2015. Potential for larger earthquakes in the East San Francisco Bay Area due to the direct connection between the Hayward and Calaveras Faults. *Geophys. Res. Lett.* 42, 2734–2741. <https://doi.org/10.1002/2015GL063575>.
- Cowan, H.A., 1989. An Evaluation of the Late Quaternary Displacements and Seismic Hazard Associated with the Hope and Kakapo Faults, Amuri district, North Canterbury, p. 282.
- Cowan, H.A., 1990. Late Quaternary displacements on the Hope Fault at Glynn Wye, North Canterbury, New Zeal. *J. Geol. Geophys.* 33, 285–293. <https://doi.org/10.1080/00288306.1990.10425686>.
- Cowan, H.A., McGlone, M.S., 1991. Late Holocene displacements and characteristic earthquakes on the Hope River segment of the Hope Fault, New Zealand. *J. R. Soc. New Zeal.* 21, 373–384. <https://doi.org/10.1080/03036758.1991.10420834>.
- Cowan, Hugh, Nicol, Andrew, Tonkin, Phillip, 1996. A comparison of historical and paleoseismicity in a newly formed fault zone and a mature fault zone, North Canterbury, New Zealand. *Journal of Geophysical Research: Solid Earth* 101 (B3), 6021–6036.
- Cox, S.C., Barrell, D.J.A., 2007. *Geology of the Aoraki Area: Scale 1:250,000 Geological Map* 15.
- Cox, S.C., Findlay, R.H., 1995. The main divide fault zone and its role in formation of the Southern Alps, New Zealand. *New Zeal. J. Geol. Geophys.* 38, 489–499. <https://doi.org/10.1080/00288306.1995.9514675>.
- Cox, S.C., Stirling, M.W., Herman, F., Gerstenberger, M., Ristau, J., 2012. Potentially active faults in the rapidly eroding landscape adjacent to the Alpine Fault, central Southern Alps, New Zealand. *Tectonics* 3. <https://doi.org/10.1029/2011TC003038>.
- Dooley, T.P., Schreurs, G., 2012. Analogue modelling of intraplate strike-slip tectonics: a review and new experimental results. *Tectonophysics* 574–575, 1–71. <https://doi.org/10.1016/j.tecto.2012.05.030>.
- Duffy, B., Quigley, M., Barrell, D.J.A., Van Dissen, R., Stahl, T., Leprince, S., McInnes, C., Bilderback, E., 2013. Fault kinematics and surface deformation across a releasing bend during the 2010 MW 7.1 Darfield, New Zealand, earthquake revealed by differential LIDAR and cadastral surveying. *Geol. Soc. Am. Bull.* 125, 420–431. <https://doi.org/10.1130/B30753.1>.

- Eaves, S.R., Anderson, B.M., Mackintosh, A.N., 2017. Glacier-based climate reconstructions for the last glacial-interglacial transition: Arthur's Pass, New Zealand (43°S). *J. Quat. Sci.* 32, 877–887. <https://doi.org/10.1002/jqs.2904>.
- Ellis, S., Wissing, A., Pfiffner, A., 2001. Strain localization as a key to reconciling experimentally derived flow-law data with dynamic models of continental collision. *Int. J. Earth Sci.* 90, 168–180. <https://doi.org/10.1007/s005310000151>.
- Eusden, J.D., Pettinga, J.R., Campbell, J.K., 2000. Structural evolution and landscape development of a collapsed transpressive duplex on the Hope Fault, North Canterbury, New Zealand. *New Zeal. J. Geol. Geophys.* 43, 391–404. <https://doi.org/10.1080/00288306.2000.9514896>.
- Eusden, J.D., Pettinga, J.R., Campbell, J.K., 2005. Structural collapse of a transpressive hanging-wall fault wedge, charwell region of the hope fault, South Island, New Zealand. *New Zeal. J. Geol. Geophys.* 48, 295–309. <https://doi.org/10.1080/00288306.2005.9515116>.
- Fedorik, J., Zwaan, F., Schreurs, G., Toscani, G., Bonini, L., Seno, S., 2019. The interaction between strike-slip dominated fault zones and thrust belt structures: insights from 4D analogue models. *J. Struct. Geol.* 122, 89–105. <https://doi.org/10.1016/j.jsg.2019.02.010>.
- Findlay, R.H., 1980. Structure of the Hooker and Copland Valleys. University of Auckland.
- Freund, R., 1971. Hope fault a strike slip fault in New Zealand. *N. Z. Geol. Surv. Bull.* 16, 49.
- Gold, R.D., DuRoss, C.B., Delano, J.E., Jibson, R.W., Briggs, R.W., Mahan, S.A., Williams, R.A., Corbett, D.R., 2019. Four major Holocene earthquakes on the reef-foot fault recorded by Sackungen in the New Madrid Seismic Zone, USA. *J. Geophys. Res. Solid Earth* 124, 3105–3126. <https://doi.org/10.1029/2018JB016806>.
- Graymer, R.W., Langenheim, V.E., Simpson, R.W., Jachens, R.C., Ponce, D.A., 2007. Relatively simple through-going fault planes at large-earthquake depth may be concealed by the surface complexity of strike-slip faults. *Geol. Soc. Lond., Spec. Publ.* 290, 189–201. <https://doi.org/10.1144/SP290.5>.
- Gutenberg, B., Richter, C.F., 1944. Frequency of earthquakes in California*. *Bull. Seismol. Soc. Am.* 34, 185–188. <https://doi.org/10.1038/156371a0>.
- Haeussler, P.J., Schwartz, D.P., Dawson, T.E., Stenner, H.D., Lienkaemper, J.J., Sherrod, B.L., Cinti, F.R., Montone, P., Craw, P.A., Crone, A.J., Personius, S.F., 2004. Surface rupture and slip distribution of the Denali and Totschunda Faults in the 3 November 2002 M 7.9 earthquake, Alaska. *Bull. Seismol. Soc. Am.* 94, S23–S52. <https://doi.org/10.1785/0120040626>.
- Haines, A.J., Wallace, L.M., 2020. New Zealand-wide geodetic strain rates using a physics-based approach. *Geophys. Res. Lett.* 47 <https://doi.org/10.1029/2019GL084606>.
- Hamling, I.J., Hreinsdóttir, S., Clark, K., Elliott, J., Liang, C., Fielding, E., Litchfield, N., Villamor, P., Wallace, L., Wright, T.J., D'Anastasio, E., Bannister, S., Burbidge, D., Denys, P., et al., 2017. Complex multifault rupture during the 2016 M w 7.8 Kaikōura earthquake, New Zealand. *Science* 356, eaam7194. <https://doi.org/10.1126/science.aam7194>.
- Hatem, Alexandra E., Dolan, James F., Zinke, Robert W., Van Dissen, Russell J., McGuire, Christopher M., Rhodes, Edward J., 2019. A 2000 Yr Paleoearthquake Record along the Conway Segment of the Hope Fault: Implications for Patterns of Earthquake Occurrence in Northern South Island and Southern North Island, New Zealand. *2000 Yr Paleoearthquake Record along the Conway Segment of the Hope Fault. Bulletin of the Seismological Society of America* 109 (6), 2216–2239.
- Herman, F., Braun, J., Dunlap, W.J., 2007. Tectonomorphic scenarios in the Southern Alps of New Zealand. *J. Geophys. Res. Solid Earth* 112. <https://doi.org/10.1029/2004JB003472>.
- Holden, C., Kaneko, Y., D'Anastasio, E., Benites, R., Fry, B., Hamling, I.J., 2017. The 2016 Kaikōura earthquake revealed by kinematic source inversion and seismic wavefield simulations: slow rupture propagation on a geometrically complex crustal fault network. *Geophys. Res. Lett.* 44, 11,320–11,328. <https://doi.org/10.1002/2017GL075301>.
- Hovius, N., Stark, C.P., Allen, P.A., 1997. Sediment flux from a mountain belt derived by landslide mapping. *Geology* 25, 231. [https://doi.org/10.1130/0091-7613\(1997\)025<0231:SFFAMB>2.3.CO;2](https://doi.org/10.1130/0091-7613(1997)025<0231:SFFAMB>2.3.CO;2).
- Howarth, J.D., Cochran, U.A., Langridge, R.M., Clark, K., Fitzsimons, S.J., Berryman, K., Villamor, P., Strong, D.T., 2018. Past large earthquakes on the Alpine Fault: paleoseismological progress and future directions. *New Zeal. J. Geol. Geophys.* 61, 309–328. <https://doi.org/10.1080/00288306.2018.1464658>.
- Ivy-Ochs, S., Schluchter, C., Kubik, P.W., Denton, G.H., 1999. Moraine exposure dates imply synchronous younger dryas glacier advances in the European Alps and in the Southern Alps of New Zealand. *Geografiska Annaler Ser. A: Phys. Geogr.* 81, 313–323. <https://doi.org/10.1111/j.0435-3676.1999.00060.x>.
- Khajavi, N., Quigley, M.C., Langridge, R.M., 2014. Influence of topography and basement depth on surface rupture morphology revealed from LIDAR and field mapping. *Hope Fault, New Zealand: Tectonophysics* 630, 265–284. <https://doi.org/10.1016/j.tecto.2014.05.032>.
- Khajavi, N., Langridge, R.M., Quigley, M.C., Smart, C., Rezanejad, A., Martín-González, F., 2016. Late Holocene rupture behavior and earthquake chronology on the Hope fault, New Zealand. *Geol. Soc. Am. Bull.* 128, 1736–1761. <https://doi.org/10.1130/B31199.1>.
- Khajavi, N., Nicol, A., Quigley, M.C., Langridge, R.M., 2018. Temporal slip-rate stability and variations on the Hope Fault, New Zealand, during the late Quaternary: *Tectonophysics* 738–739, 112–123. <https://doi.org/10.1016/j.tecto.2018.05.001>.
- Kinakin, D., Stead, D., 2005. Analysis of the distributions of stress in natural ridge forms: implications for the deformation mechanisms of rock slopes and the formation of sackung. *Geomorphology* 65, 85–100. <https://doi.org/10.1016/j.geomorph.2004.08.002>.
- Knuepfer, P.L.K., 1992. Temporal variations in latest Quaternary slip across the Australian-Pacific Plate Boundary, northeastern South Island, New Zealand. *Tectonics* 11, 449–464. <https://doi.org/10.1029/91TC02890>.
- Komura, K., Kaneda, H., Kashiwara, S., Nishio, T., Kojima, S., 2017. Deformation History of Sackung Features Concentrated Around the Northern Tip of the Active Neodani Fault, Central Japan Keitaro, pp. 180–181. <https://doi.org/10.21420/G2H061>.
- Koons, P.O., 1990. The two-sided orogen: Collision and erosion from the sand box to the Southern Alps, New Zealand. *Geology* 18, 679–682. [https://doi.org/10.1130/0091-7613\(1990\)018<0679:TSOCAE>2.3.CO;2](https://doi.org/10.1130/0091-7613(1990)018<0679:TSOCAE>2.3.CO;2).
- Koons, P.O., Norris, R.J., Craw, D., Cooper, A.F., 2003. Influence of exhumation of the structural evolution of transpressional plate boundaries: an example from the Southern Alps, New Zealand. *Geology* 31, 3–6. [https://doi.org/10.1130/0091-7613\(2003\)031<0003:IOEOTS>2.0.CO;2](https://doi.org/10.1130/0091-7613(2003)031<0003:IOEOTS>2.0.CO;2).
- Korup, O., McSaveney, M.J., Davies, T.R.H., 2004. Sediment generation and delivery from large historic landslides in the Southern Alps, New Zealand. *Geomorphology* 61, 189–207. <https://doi.org/10.1016/j.geomorph.2004.01.001>.
- Korup, O., Clague, J.J., Hermanns, R.L., Hewitt, K., Strom, A.L., Weidinger, J.T., 2007. Giant landslides, topography, and erosion. *Earth Planet. Sci. Lett.* 261, 578–589. <https://doi.org/10.1016/j.epsl.2007.07.025>.
- Krantz, R.W., 1991. Measurements of friction coefficients and cohesion for faulting and fault reactivation in laboratory models using sand and sand mixtures. *Tectonophysics* 188, 203–207. [https://doi.org/10.1016/0040-1951\(91\)90323-K](https://doi.org/10.1016/0040-1951(91)90323-K).
- Landgraf, A., Ballato, P., Strecker, M.R., Friedrich, A., Tabatabaei, S.H., Shahpasandzadeh, M., 2009. Fault-kinematic and geomorphic observations along the North Tehran Thrust and Moshafasham Fault, Alborz mountains Iran: implications for fault-system evolution and interaction in a changing tectonic regime. *Geophys. J. Int.* 177, 676–690. <https://doi.org/10.1111/j.1365-246X.2009.04089.x>.
- Langridge, R.M., Berryman, K.R., 2005. Morphology and slip rate of the Hurunui section of the Hope Fault, South Island, New Zealand. *New Zeal. J. Geol. Geophys.* 48, 43–57. <https://doi.org/10.1080/00288306.2005.9515097>.
- Langridge, R.M., Campbell, J.K., Hill, N., Pere, V., Pope, J., Pettinga, J.R., Estrada, B., Berryman, K., 2003. Paleoseismology and slip rate of the Conway Segment of the Hope Fault at Greenburn Stream, South Island, New Zealand. *Ann. Geophys.* 46, 1119–1140. <https://doi.org/10.4401/ag-3449>.
- Langridge, R.M., Villamor, P., Basili, R., Almond, P., Martinez-Diaz, J.J., Canora, C., 2010. Revised slip rates for the Alpine fault at Incheon: implications for plate boundary kinematics of South Island, New Zealand. *Lithosphere* 2, 139–152. <https://doi.org/10.1130/L88.1>.
- Langridge, R.M., Almond, P.C., Duncan, R.P., 2013. Timing of late Holocene paleoearthquakes on the Hurunui segment of the Hope fault: implications for plate boundary strain release through South Island, New Zealand. *Geol. Soc. Am. Bull.* 125, 756–775. <https://doi.org/10.1130/B30674.1>.
- Langridge, R.M., Ries, W.F., Farrier, T., Barth, N.C., Khajavi, N., De Pascale, G.P., 2014. Developing sub 5-m LIDAR DEMs for forested sections of the Alpine and Hope faults, South Island, New Zealand: Implications for structural interpretations. *J. Struct. Geol.* 64, 53–66. <https://doi.org/10.1016/j.jsg.2013.11.007>.
- Langridge, R.M., Ries, W., Litchfield, N., Villamor, P., Van Dissen, R., Barrell, D., Rattenbury, M., Heron, D., Haubrock, S., Townsend, D., Lee, J., Berryman, K., Nicol, A., Cox, S., et al., 2016. The New Zealand active Faults Database. *N. Z. J. Geol. Geophys.* 59, 86–96. <https://doi.org/10.1080/00288306.2015.1112818>.
- Langridge, R.M., Ries, W.F., Dolan, J.F., Schermer, E.R., Siddoway, C., 2017. Slip rate estimates and slip gradient for the Alpine Fault at Calf Paddock, Maruia River, New Zealand. *New Zeal. J. Geol. Geophys.* 60, 73–88. <https://doi.org/10.1080/00288306.2016.1275707>.
- Langridge, R.M., Villamor, P., Howarth, J.D., Ries, W.F., Clark, K.J., Litchfield, N.J., 2020. Reconciling an Early Nineteenth-Century Rupture of the Alpine Fault at a Section End, Toaroha River, Westland, New Zealand. *Bulletin of the Seismological Society of America*. <https://doi.org/10.1785/0120200116>.
- Leitner, B., Eberhart-Phillips, D., Anderson, H., Nabelek, J.L., 2001. A focused look at the Alpine fault, New Zealand: seismicity, focal mechanism, and stress observations. *J. Geophys. Res.* 106, 2193–2220.
- Lensen, G.J., 1976. Earth deformation in relation to town planning in New Zealand. *Bull. Int. Assoc. Eng. Geol.* 13, 241–247. <https://doi.org/10.1007/BF02634800>.
- Li, Z., Bruhn, R.L., Pavlis, T.L., Vorkink, M., Zeng, Z., 2010. Origin of sackung uphill-facing scarps in the Saint Elias orogen, Alaska: LIDAR data visualization and stress modeling. *Geol. Soc. Am. Bull.* 122, 1585–1599. <https://doi.org/10.1130/B30019.1>.
- Litchfield, N., Van Dissen, R., Sutherland, R., Barnes, P., Cox, S., Norris, R., Beavan, R., Langridge, R.M., Villamor, P., Berryman, K., Stirling, M., Nicol, A., Nodder, S., Lamarche, G., et al., 2014. A model of active faulting in New Zealand. *N. Z. J. Geol. Geophys.* 57, 32–56. <https://doi.org/10.1080/00288306.2013.854256>.
- Little, T.A., Jones, A., 1998. Seven million years of strike-slip and related off-fault deformation, northeastern Marlborough fault system, South Island, New Zealand. *Tectonics* 17, 285–302. <https://doi.org/10.1029/97TC03148>.
- Little, T.A., Cox, S., Vry, J.K., Batt, G., 2005. Variations in exhumation level and uplift rate along the oblique-slip Alpine fault, central Southern Alps, New Zealand. *Geol. Soc. Am. Bull.* 117, 707. <https://doi.org/10.1029/B25500.1>.
- Lock, J., Kelsey, H., Furlong, K., Woolace, A., 2006. Late Neogene and Quaternary landscape evolution of the northern California Coast Ranges: evidence for Mendocino triple junction tectonics. *Geol. Soc. Am. Bull.* 118, 1232–1246. <https://doi.org/10.1130/B25885.1>.
- Manighetti, I., Perrin, C., Dominguez, S., Garambois, S., Gaudemer, Y., Malavieille, J., Matteo, L., Delor, E., Vitard, C., Beauprêtre, S., 2015. Recovering paleoearthquake slip record in a highly dynamic alluvial and tectonic region (Hope Fault, New Zealand) from airborne lidar. *J. Geophys. Res. Solid Earth* 120, 4484–4509. <https://doi.org/10.1002/2014JB011787>.

- Mason, D.P.M., Little, T.A., Van Dissen, R.J., 2006. Rates of active faulting during late Quaternary fluvial terrace formation at Saxton River, Awatere fault, New Zealand. *Geol. Soc. Am. Bull.* 118, 1431–1446. <https://doi.org/10.1130/B25961.1>.
- Massey, C., Townsend, D., Rathje, E., Allstadt, K.E., Lukovic, B., Kaneko, Y., Bradley, B., Wartman, J., Jibson, R.W., Petley, D.N., Horspool, N., Hamling, I., Carey, J., Cox, S., et al., 2018. Landslides triggered by the 14 November 2016 Mw 7.8 Kaikōura earthquake, New Zealand. *Bull. Seismol. Soc. Am.* 108, 1630–1648. <https://doi.org/10.1785/0120170305>.
- McClay, K., Whitehouse, P., Dooley, T., Richards, M., 2004. 3D evolution of fold and thrust belts formed by oblique convergence. *Mar. Pet. Geol.* 21, 857–877. <https://doi.org/10.1016/j.marpetgeo.2004.03.009>.
- McGill, S.F., Owen, L.A., Weldon, R.J., Kendrick, K.J., 2013. Latest Pleistocene and Holocene slip rate for the San Bernardino strand of the San Andreas fault, Plunge Creek, Southern California: implications for strain partitioning within the southern San Andreas fault system for the last ~35 k.y. *Geol. Soc. Am. Bull.* 125, 48–72. <https://doi.org/10.1130/B30647.1>.
- McKay, A., 1890. On the Earthquakes of September 1888 in the Amuri and Marlborough Districts of the South Island: New Zealand. *Geological Survey Report of Geological Explorations* 20, 1–16.
- Michailos, K., Smith, E.G.C., Chamberlain, C.J., Savage, M.K., Townend, J., 2019. Variations in seismogenic thickness along the Central Alpine Fault, New Zealand, revealed by a decade's relocated microseismicity. *Geochim. Geophys. Geosyst.* 20, 470–486. <https://doi.org/10.1029/2018GC007743>.
- Michailos, K., Warren-Smith, E., Savage, M.K., Townend, J., 2020. Detailed spatiotemporal analysis of the tectonic stress regime near the central Alpine Fault, New Zealand. *Tectonophysics* 775, 228205. <https://doi.org/10.1016/j.tecto.2019.228205>.
- Morton, D.M., Matti, J.C., 1993. Extension and contraction within an evolving divergent strike-slip fault complex: the San Andreas and San Jacinto fault zones at their convergence in southern California. *Geol. Soc. Am.* 1993, 332.
- Mouslopoulou, V., Nicol, A., Little, T.A., Walsh, J.J., 2007a. Displacement transfer between intersecting regional strike-slip and extensional fault systems. *J. Struct. Geol.* 29, 100–116. <https://doi.org/10.1016/j.jsg.2006.08.002>.
- Mouslopoulou, V., Nicol, A., Little, T.A., Walsh, J.J., 2007b. Terminations of large strike-slip faults: an alternative model from New Zealand. *Geol. Soc. Lond. Sp. Publ.* 290, 387–415. <https://doi.org/10.1144/SP290.15>.
- Nathan, S., Rattenbury, M., Suggate, R.P., 2002. *Geology of the Graymouth Area*, p. 58.
- Nicol, A., Wise, D.U., 1992. Paleostress adjacent to the Alpine Fault of New Zealand: fault, vein, and stylolite data from the Doctors Dome Area. *J. Geophys. Res.* 97, 17685. <https://doi.org/10.1029/92JB01201>.
- Nicol, A., Khajavi, N., Pettinga, J.R., Fenton, C., Stahl, T., Bannister, S., Pedley, K., Hyland-Brook, N., Bushell, T., Hamling, I., Ristau, J., Noble, D., McColl, S.T., 2018. Preliminary geometry, displacement, and kinematics of fault ruptures in the epicentral region of the 2016 Mw 7.8 Kaikōura, New Zealand, Earthquake. *Bull. Seismol. Soc. Am.* 108, 1521–1539. <https://doi.org/10.1785/0120170329>.
- Niemi, N.A., Buscher, J.T., Spotila, J.A., House, M.A., Kelley, S.A., 2013. Insights from low-temperature thermochronometry into transpressional deformation and crustal exhumation along the San Andreas fault in the western Transverse Ranges, California. *Tectonics* 32, 1602–1622. <https://doi.org/10.1002/2013TC003377>.
- Norris, R.J., Cooper, A.F., 1995. Origin of small-scale segmentation and transpressional thrusting along the Alpine fault, New Zealand. *Geol. Soc. Am. Bull.* 107, 231. [https://doi.org/10.1130/0016-7606\(1995\)107<0231:OOSSSA>2.3.CO;2](https://doi.org/10.1130/0016-7606(1995)107<0231:OOSSSA>2.3.CO;2).
- Norris, R.J., Cooper, A.F., 2001. Late Quaternary slip rates and slip partitioning on the Alpine Fault, New Zealand. *J. Struct. Geol.* 23, 507–520. [https://doi.org/10.1016/S0191-8141\(00\)00122-X](https://doi.org/10.1016/S0191-8141(00)00122-X).
- Öncel, A.O., Wilson, T.H., Nishizawa, O., 2001. Size scaling relationships in the active fault networks of Japan and their correlation with Gutenberg-Richter b values. *J. Geophys. Res. Solid Earth* 106, 21827–21841. <https://doi.org/10.1029/2000jb900408>.
- Parsons, T., Field, E.H., Page, M.T., Milner, K., 2012. Possible Earthquake Rupture Connections on Mapped California Faults Ranked by calculated Coulomb linking Stresses. *Bull. Seismol. Soc. Am.* 102, 2667–2676. <https://doi.org/10.1785/0120110349>.
- Peacock, D.C.P., Nixon, C.W., Rotevatn, A., Sanderson, D.J., Zuluaga, L.F., 2017. Interacting faults. *J. Struct. Geol.* 97, 1–22. <https://doi.org/10.1016/j.jsg.2017.02.008>.
- Pere, V., 2009. *Antiscarp Initiation and Evolution*. University of Canterbury, p. 203.
- Pettinga, J.R., Wise, D.U., 1994. Paleostress adjacent to the Alpine fault: broader implications from fault analysis near Nelson, South Island, New Zealand. *J. Geophys. Res. Solid Earth* 99, 2727–2736. <https://doi.org/10.1029/93JB02900>.
- Pettinga, J.R., Yetton, M.D., Van Dissen, R.J., Downes, G., 2001. Earthquake source identification and characterisation for the Canterbury region, South Island, New Zealand. *Bull. N. Z. Soc. Earthq. Eng.* 34, 282–317. <https://doi.org/10.5459/bnzsee.34.4.282-317>.
- Quigley, M.C., Jiménez, A., Duffy, B., King, T.R., 2019. Physical and statistical behavior of multifault earthquakes: Darfield Earthquake Case Study, New Zealand. *J. Geophys. Res. Solid Earth* 124, 4788–4810. <https://doi.org/10.1029/2019JB017508>.
- Ratchkovski, Natalia A., Wiemer, Stefan, Hansen, Roger A., 2004. Seismotectonics of the central Denali fault, Alaska, and the 2002 Denali fault earthquake sequence. *Bulletin of the Seismological Society of America* 94 (6B), S156–S174.
- Rattenbury, M.S., 1987. Fraser Complex and Alpine Fault Tectonics, Central Westland. University of Otago, New Zealand. <http://hdl.handle.net/10523/3459>.
- Rattenbury, M.S., Vidanovich, P., 2018. The aeromagnetic expression of New Zealand's Alpine Fault: regional displacement and entrainment of igneous rock. *New Zeal. J. Geol. Geophys.* 61, 272–282. <https://doi.org/10.1080/00288306.2018.1464031>.
- Rattenbury, M.S., Townsend, D., Johnston, M.R., 2006. *Geology of the Kaikōura Area: Scale 1:250,000 Geological Map* 13.
- Reber, J.E., Cooke, M.L., Dooley, T.P., 2020. What model material to use? A Review on rock analogs for structural geology and tectonics. *Earth-Sci. Rev.* 202, 103107. <https://doi.org/10.1016/j.earscirev.2020.103107>.
- Robinson, R., 2004. Potential earthquake triggering in a complex fault network: the northern South Island, New Zealand. *Geophys. J. Int.* 159, 734–748. <https://doi.org/10.1111/j.1365-246X.2004.02446.x>.
- Robinson, T.R., Davies, T.R.H., Wilson, T.M., Orchiston, C., 2016. Coseismic landsliding estimates for an Alpine Fault earthquake and the consequences for erosion of the Southern Alps, New Zealand. *Geomorphology* 263, 71–86. <https://doi.org/10.1016/j.geomorph.2016.03.033>.
- Rosas, F.M., Duarte, J.C., Neves, M.C., Terrinha, P., Silva, S., Matias, L., Gràcia, E., Bartolome, R., 2012. Thrust–wrench interference between major active faults in the Gulf of Cadiz (Africa–Eurasia plate boundary, offshore SW Iberia): tectonic implications from coupled analog and numerical modeling. *Tectonophysics* 548–549, 1–21. <https://doi.org/10.1016/j.tecto.2012.04.013>.
- Rosas, F.M., Duarte, J.C., Schellart, W.P., Tomás, R., Grigorova, V., Terrinha, P., 2015. Analogue modelling of different angle thrust–wrench fault interference in a brittle medium. *J. Struct. Geol.* 74, 81–104. <https://doi.org/10.1016/j.jsg.2015.03.005>.
- Rosser, B.J., Carey, J.M., 2017. Comparison of landslide inventories from the 1994 Mw 6.8 Arthurs Pass and 2015 Mw 6.0 Wilberforce earthquakes, Canterbury, New Zealand. *Landslides* 14, 1171–1180. <https://doi.org/10.1007/s10346-017-0797-8>.
- Rundle, John B., 1989. Derivation of the complete Gutenberg-Richter magnitude-frequency relation using the principle of scale invariance. *Journal of Geophysical Research: Solid Earth* 94 (B9), 12337–12342. <https://doi.org/10.1029/1989JB005844>.
- Rundle, J.B., Rundle, P.B., Donnellan, A., Fox, G., 2004. Gutenberg-Richter statistics in topologically realistic system-level earthquake stress–evolution simulations. *Earth Planets Space* 56, 761–771. <https://doi.org/10.1186/BF03353084>.
- Savage, W.Z., Varnes, D.J., 1987. Mechanics of gravitational spreading of steep-sided ridges («sackung»). *Bull. Int. Assoc. Eng. Geol.* 35, 31–36. <https://doi.org/10.1007/BF02590474>.
- Scholz, C.H., Ando, R., Shaw, B.E., 2010. The mechanics of first order splay faulting: the strike-slip case. *J. Struct. Geol.* 32, 118–126. <https://doi.org/10.1016/j.jsg.2009.10.007>.
- Schwartz, D.P., Haeussler, P.J., Seitz, G.G., Dawson, T.E., 2012. Why the 2002 Denali fault rupture propagated onto the Totschunda fault: Implications for fault branching and seismic hazards. *J. Geophys. Res. Solid Earth* 117. <https://doi.org/10.1029/2011JB008918>.
- Sheridan, M., 2014. The Effects of an Alpine Fault Earthquake on the Taramakau River, South Island New Zealand. University of Canterbury, p. 122. <http://hdl.handle.net/10092/10253>.
- Shulmeister, J., Thackray, G.D., Rittenour, T.M., Fink, D., Patton, N.R., 2019. The timing and nature of the last glacial cycle in New Zealand. *Quat. Sci. Rev.* 206, 1–20. <https://doi.org/10.1016/j.quascirev.2018.12.020>.
- Sieh, K., Jones, L., Hauksson, E., Hudnut, K., Eberhart-Phillips, D., Heaton, T., Hough, S., Hutton, K., Kanamori, H., Lilje, A., Lindvall, S., McGill, S.F., Mori, J., Rubin, C., et al., 1993. Near-Field Investigations of the Landers Earthquake Sequence, April to July 1992. *Science* 260, 171–176. <https://doi.org/10.1126/science.260.5105.171>.
- Silberling, N.J., Nichols, K.M., Bradshaw, J.D., Blome, C.D., 1988. Limestone and chert in tectonic blocks from the Esk Head subterranean, South Island, New Zealand. *Geol. Soc. Am. Bull.* 100, 1213–1223. [https://doi.org/10.1130/0016-7606\(1988\)100<1213:LACITB>2.3.CO;2](https://doi.org/10.1130/0016-7606(1988)100<1213:LACITB>2.3.CO;2).
- Spotila, J.A., Anderson, K.B., 2004. Fault interaction at the junction of the Transverse Ranges and Eastern California shear zone: a case study of intersecting faults. *Tectonophysics* 379, 43–60. <https://doi.org/10.1016/j.tecto.2003.09.016>.
- Spotila, J.A., Niemi, N., Brady, R., House, M., Buscher, J., Osokin, M., 2007. Long-term continental deformation associated with transpressive plate motion: the San Andreas fault. *Geology* 35, 967. <https://doi.org/10.1130/G23816A.1>.
- Stirling, M., McVerry, G., Gerstenberger, M., Litchfield, N., Van Dissen, R., Berryman, K., Barnes, P., Wallace, L., Villamor, P., Langridge, R., Lamarche, G., Nodder, S., Reyners, M., Bradley, B., et al., 2012. National seismic hazard model for New Zealand: 2010 Update. *Bull. Seismol. Soc. Am.* 102, 1514–1542. <https://doi.org/10.1785/0120110170>.
- Sutherland, R., Eberhart-Phillips, D., Harris, R.A., Stern, T., Beavan, J., Ellis, S., Henrys, S., Cox, S., Norris, R.J., Berryman, K.R., Townend, J., Bannister, S., Pettinga, J., Leitner, B., et al., 2007. Do great earthquakes occur on the Alpine Fault in central South Island, New Zealand? In: *A Continental Plate Boundary: Tectonics at South Island, New Zealand*, v. 175, pp. 235–251. <https://doi.org/10.1029/175GM12>.
- Tait, A., Henderson, R., Turner, R., Zheng, X., 2006. Thin plate smoothing spline interpolation of daily rainfall for New Zealand using a climatological rainfall surface. *Int. J. Climatol.* 26, 2097–2115. <https://doi.org/10.1002/joc.1350>.
- Tibaldi, A., Bistacchi, A., Pasquaré, F.A., Vezzoli, L., 2006. Extensional tectonics and volcano lateral collapses: insights from Ollague volcano (Chile-Bolivia) and analogue modelling. *Terra Nova* 18, 282–289. <https://doi.org/10.1111/j.1365-3121.2006.00691.x>.
- Townend, J., Sherburn, S., Arnold, R., Boese, C., Woods, L., 2012. Three-dimensional variations in present-day tectonic stress along the Australia–Pacific plate boundary in New Zealand. *Earth Planet. Sci. Lett.* 353–354, 47–59. <https://doi.org/10.1016/j.epsl.2012.08.003>.
- Upton, P., Craw, D., James, Z., Koons, P.O., 2004. Structure and late Cenozoic tectonics of the southern Two Thumb range, mid Canterbury, New Zealand. *New Zeal. J. Geol. Geophys.* 47, 141–153. <https://doi.org/10.1080/00288306.2004.9515043>.

- van Dissen, R., Nicol, A., 2009. Mid-late Holocene paleoseismicity of the eastern Clarence Fault, Marlborough, New Zealand. *New Zeal. J. Geol. Geophys.* 52, 195–208. <https://doi.org/10.1080/00288300909509886>.
- Van Dissen, R., Yeats, R.S., 1991. Hope fault, Jordan thrust, and uplift of the Seaward Kaikoura Range, New Zealand. *Geology* 19, 393. [https://doi.org/10.1130/0091-7613\(1991\)019<0393:HFJTAU>2.3.CO;2](https://doi.org/10.1130/0091-7613(1991)019<0393:HFJTAU>2.3.CO;2).
- van Gent, H., Urai, J.L., 2020. Abutting faults: a case study of the evolution of strain at Courthouse branch point, Moab Fault, Utah. *Solid Earth* 11, 513–526. <https://doi.org/10.5194/se-11-513-2020>.
- Wakabayashi, J., Hengesh, J.V., Sawyer, T.L., 2004. Four-dimensional transform fault processes: progressive evolution of step-overs and bends. *Tectonophysics* 392, 279–301. <https://doi.org/10.1016/j.tecto.2004.04.013>.
- Walcott, R.I., 1998. Modes of oblique compression: Late Cenozoic tectonics of the South Island of New Zealand. *Rev. Geophys.* 36, 1–26. <https://doi.org/10.1029/97RG03084>.
- Wallace, L.M., Beavan, J., McCaffrey, R., Berryman, K., Denys, P., 2007. Balancing the plate motion budget in the South Island, New Zealand using GPS, geological and seismological data. *Geophys. J. Int.* 168, 332–352. <https://doi.org/10.1111/j.1365-246X.2006.03183.x>.
- Watt, J.T., Ponce, D.A., Graymer, R.W., Jachens, R.C., Simpson, R.W., 2014. Subsurface geometry of the San Andreas-Calaveras fault junction: influence of serpentinite and the Coast Range Ophiolite. *Tectonics* 33, 2025–2044. <https://doi.org/10.1002/2014TC003561>.
- Wesnousky, S.G., 1999. Crustal deformation processes and the stability of the Gutenberg-Richter relationship. *Bull. Seismol. Soc. Am.* 89, 1131–1137.
- West Coast Regional Council, 2017. West Coast Imagery (2015–2017). <https://gis.westcoast.govt.nz/arcgis/rest/services/Basemaps/WestCoastImagery2016/MapServer> (Accessed July 2020).
- Wood, R.A., Pettinga, J.R., Bannister, S., Lamarche, G., McMorran, T.J., 1994. Structure of the Hanmer strike-slip basin, Hope fault, New Zealand. *Geol. Soc. Am. Bull.* 106, 1459–1473. [https://doi.org/10.1130/0016-7606\(1994\)106<1459:SOTHSS>2.3.CO;2](https://doi.org/10.1130/0016-7606(1994)106<1459:SOTHSS>2.3.CO;2).
- Yang, J.S., 1991. The Kakapo Fault — A major active dextral fault in the central North Canterbury - Buller regions of New Zealand. *N. Z. J. Geol. Geophys.* 34, 137–143. <https://doi.org/10.1080/00288306.1991.9514451>.
- Yang, J.S., 1992. Landslide mapping and major earthquakes on the Kakapo fault, South Island, New Zealand. *J. R. Soc. New Zeal.* 22, 205–212. <https://doi.org/10.1080/03036758.1992.10426557>.
- Zachariasen, J., Sieh, K., 1995. The transfer of slip between two en echelon strike-slip faults: a case study from the 1992 Landers earthquake, southern California. *J. Geophys. Res. Solid Earth* 100, 15281–15301. <https://doi.org/10.1029/95JB00918>.
- Zachariasen, J., Berryman, K., Langridge, R.M., Prentice, C., Rymer, M., Stirling, M., Villamor, P., 2006. Timing of late Holocene surface rupture of the Wairau Fault, Marlborough, New Zealand. *New Zeal. J. Geol. Geophys.* 49, 159–174. <https://doi.org/10.1080/00288306.2006.9515156>.
- Žalohar, J., 2012. Cosserat analysis of interactions between intersecting faults; the wedge faulting. *J. Struct. Geol.* 37, 105–123. <https://doi.org/10.1016/j.jsg.2012.01.023>.
- Zischinsky, U., 1969. Über Sackungen. *Rock Mech.* 1, 30–52. <https://doi.org/10.1007/BF01247356>.